AIMS Materials Science, 5(3): 349–401.
DOI: 10.3934/matersci.2018.3.349
Received: 26 January 2018
Accepted: 15 April 2018
Published: 27 April 2018

http://www.aimspress.com/journal/Materials

Review

V_2O_5 thin films for energy storage and conversion

Alain Mauger* and Christian M. Julien

Sorbonne Universités, Institut de Minéralogie, de Physique des Matériaux et de Cosmologie (IMPMC), UMR 7590, 4 place Jussieu, 75252 Paris, France

* **Correspondence:** Email: alain.mauger@upmc.fr.

Abstract: V_2O_5 is one of the best material for many applications. Progress is currently made to improve its performance for use as a sensor, or an electrode, or smart window, electrochromic device, supercapacitor, photovoltaic applications among others. In this work, we review the progress that has been done these recent years, in relation to the mode of preparation of the V_2O_5 films. The results outline the complex relationship between the synthesis and the properties, which should serve as a guide for further research on the dependence of the best synthesis process on the type of application that is targeted.

Keywords: vanadium pentoxide; thin films; surface; intercalation; energy storage

1. Introduction

Vanadium is sparsely distributed in the earth's crust. It is found at an average concentration of 150 mg kg^{-1} in mineral ores and in the range of 3–300 mg kg^{-1} in soil. Vanadium pentoxide, the highest oxidation state 5+ of vanadium, has been known for more than a century. In December 1867, as a part of his Bakerian lecture to the Royal Society, the British chemist Sir Henry Roscoe outlined the multiple oxidation states of binary oxides of vanadium and set the end-member "vanadic acid" V_2O_5 [1]. The first V_2O_5 gel was described by the French chemist Ditte in 1885 [2]. The natural occurrence (50%) of V_2O_5 is found in flue-gas deposits from oil-fired furnaces and residues from elemental phosphate plants. However, V_2O_5 mineral is rare; *shcherbinaite* V_2O_5 (orthorhombic crystal system) is found on the walls of volcanic fissures [3] and *navajoite* is a mineral trihydrate $V_2O_5{\cdot}3H_2O$ (monoclinic structure). The *titanoferous magnetite* ore in lump form contains approximately 1.5–1.7% vanadium pentoxide.

The structure of crystal isolated from fused V_2O_5 was first elucidated by Katelaar [4] as a rhombic unit cell containing two molecules of V_2O_5. Refinements were further done by Byström et al. [5] who established the orthorhombic layered structure of V_2O_5 with *Pmmn* space group. In 1961, Bachmann et al. [6] redetermined the crystal structure of V_2O_5 and reported its lattice parameters a = 11.510 Å, b = 4.369 Å, c = 3.563 Å. Their structural description is as follows: "*the structure is built up from distorted trigonal bipyramidal coordination polyhedral of O around V, which share edges to form zigzag double chains along [001] and are cross-linked along [100] through shared corners, thus forming sheets in the zz plane*". More recently, Enjalbert and Galy [7] proposed the bonding interactions of van der Waals type between two-dimensional V_2O_5 slabs and stated the presence of "square pyramid" instead of trigonal bipyramid. Ramana et al. [8] and Julien et al. [9] have described the easy cleavage along the (001) plane due to the weak interaction between V_2O_5 layers. Three V_2O_5 polymorphs have been identified as α-, β-V_2O_5, which crystallize with the orthorhombic and tetragonal structure, respectively, and the rutile-type δ-V_2O_5, which is a modification of β-V_2O_5 (space group $C12/c1$) [10]. Recently, Parija et al. [11] evaluated the metastable polymorphs including γ'-, δ'- and ρ'-phase of V_2O_5 using density functional theory calculations.

Here, we review the properties of V_2O_5 thin films employed in energy storage and conversion systems, which were prepared with a variety of deposition options. Numerous works prior 2001 have been devoted to the studies of synthesis, physical characterizations and electrochemical performances of films used as either cathode in all-solid-state batteries [12–15] or electrode of electrochromic devices [16]. Recently, Mo-doped V_2O_5 thin film has been studied as an electrode of supercapacitors [17]. This is an illustration of the increasing interest in this material in the recent years for many applications, sustained by numerous works that are reviewed here.

This review paper is organized as follows. In Section 2, we summarize the techniques used for the preparation of films and discuss the structure and morphology of V_2O_5 related to the synthesis conditions (temperature, partial pressure, substrate, etc.). Section 3 is devoted to the physical properties of V_2O_5 thin films; structure, morphology, vibrational spectroscopy, elemental analysis, electrical properties and intercalation process are considered. In the following Sections 4 and 5, doped V_2O_5 thin films and composite films are treated, respectively. Finally, Section 6 is devoted to the applications in the field of energy, for which V_2O_5 thin films are used as electrode materials in lithium microbatteries, electrochromic devices, sensors and supercapacitors.

2. Thin film synthesis

The structure and morphology of vanadium oxide films are intimately related to the deposition method and the operating conditions. As the direct growth of crystalline V_2O_5 films is very difficult except in the cases of some sub-stoichiometric VO_x oxides, an annealing process of the as-prepared films is required in air and high temperature. In this section we describe the different evaporation methods and provide some typical examples for each technique used. Note that the choice of a deposition method depends of the thin film application. For instance, electrodeposition [18], reactive sputtering [19], sol-gel [20], hydrothermal method [21], doctor-blade route [22] were carried out for electrochromic V_2O_5 films that requests large surface coatings. The reader will find supplementary data in the review by Beke [23]. During the deposition process in vacuum or in a reducing atmosphere, the removal of oxygen atoms occurs from the film network when V_2O_5 is heated above

its melting point that induces the formation of defects or reduced VO_x phases. Consequently, the structural and morphological disorders and phase instability can be controlled using appropriate deposition parameters.

2.1. Thermal deposition

The thermal evaporation technique is the simplest method based in the production of flux of vapor in a high vacuum chamber (pressure 100 mPa) to form thin films without the presence of catalyst. In this method, the substance is evaporated by means of resistive heating. Generally, the raw powder is placed in a molybdenum boat heated at T_{boat}. The modifications of the structure, stoichiometry and morphology of the deposited films are obtained by varying the substrate temperature T_s, the flow of reactive gases (in cm^3 min^{-1} at standard pressure and temperature, expressed as "sccm" hereafter) and the duration of the target evaporation. For example, thermally evaporated polycrystalline V_2O_5 films (10–20 nm grain size) were fabricated using T_{boat} = 650 ℃ for 6 h with gas flow 13 sccm Ar + 50% O_2 [24]. The nature of the substrate is an important factor to obtain films with preferential orientation [25]. V_2O_5 films deposited on silicon (111) wafers by vacuum thermal evaporation were amorphous when deposited at $T_s \leq 200$ ℃, while polycrystalline at $T_s \geq 300$ ℃. This later temperature is optimum for V_2O_5 films strongly oriented with (001) planes parallel to the substrate [26]. Nanostructured V_2O_5 thin films (25 nm grain size) thermally deposited onto Ni substrates at T_s = 300 ℃ show preferential (001) orientation. These films have pseudocapacitance of 730 mF cm^{-2} at current density of 1 mA cm^{-2} and charge transfer resistance of 7.5 Ω [27]. The thermally evaporated V_2O_5 films at T_s = 25 ℃, 100-nm thick, crystallized after annealing process at 500 ℃ with grain size 26 nm and exhibited an electrical conductivity of 5.5 S cm^{-1} (activation energy of 0.16 eV) [28] and optical bandgap of 2.8 eV.

2.2. Flash-evaporation

In the flash-evaporation method, the powders are placed in a reservoir and poured drop by drop into the boat heated at T_{boat} to ensure the vaporization. This process allows the control of the vaporization rate and preserves any decomposition of the starting material before evaporation [29]. It was demonstrated that V_2O_5 flash-evaporated films are more homogeneous [30]. Flash-evaopration was also used for depositing $Li_xV_2O_5$ [31]. Polycrystalline V_2O_5 flash-evaporated films have been investigated as a function of the deposition conditions: various substrates, substrate temperature (T_s), oxygen partial pressure (pO_2) and post-annealing treatment (T_a) [9]. Figure 1 presents the evolution of the O/V ratio as a function of the temperature of the molybdenum boat [32]. Films with the best stoichiometry O/V = 2.497 were obtained for T_{boat} in the range 910–980 ℃. However, properties of flash-evaporated films are strongly dependent on the deposition "quenching rate" ΔT, which is the difference in temperature between the melt and the substrate ($\Delta T = T_a - T_s$).

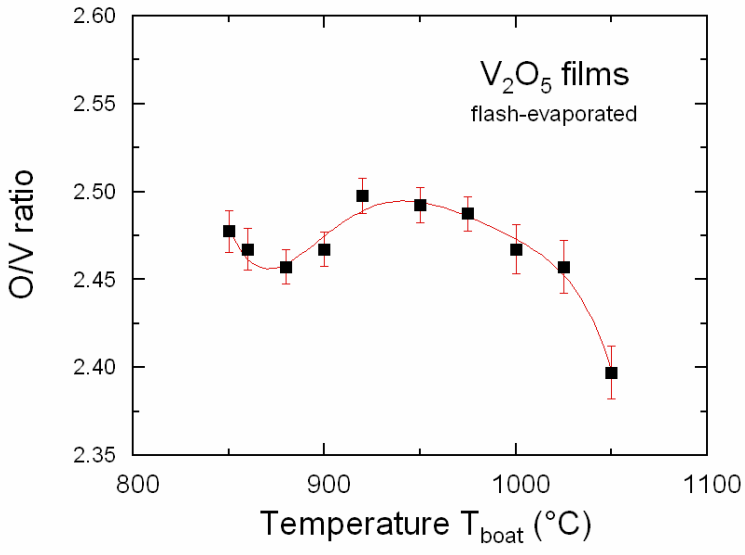

Figure 1. Evolution of the O/V ratio in flash-evaporated V_2O_5 films as a function of the boat temperature (From Ref. [32]).

2.3. Chemical vapor deposition (CVD)

Chemical vapor deposition (CVD) is a versatile technique that consists of an evaporator and a deposition system. The precursor solution is vaporized into a reactor which acts as a flash evaporation system. The vapor condenses in a cold-wall reactor in which the substrate placed in the central zone is maintained at constant temperature T_s [33]. This technique has been successfully carried out to grow V_2O_5 films using pure or diluted triisopropoxyvanadium oxide $VO(OC_3H_7)_3$ precursor [34]. Typical V_2O_5 film 240 nm thick was formed at T_s = 300 °C in the total pressure p_t = 2400 Pa with a flow of O_2 of 100 sccm. V_3O_7 and V_4O_7 films are deposited when p_t decreases to 1200 Pa, while V_6O_{13} films are formed at T_s = 350 °C and O_2 flow rate of 120 sccm. Highly crystallized films (94 nm crystallite size) were obtained after post-annealing at 500 °C for 2 h in O_2 atmosphere with a slow cooling process to insure a good adherence on substrate. Plasma-enhanced chemical vapor deposition (PE-CVD) is a method for large scale film deposition. In this technique, glow discharge creating high-energy electrons ionize gaseous molecules and generate chemically reactive ions. Heat-treated (500 °C for 2 h) films deposited by CVD technique onto Pt foil are highly structured with homogeneous and smooth surfaces as shown in Figure 2a. The coherence domains along the *a*- and *c*-axis are L_{200} = 71 nm and L_{001} = 36 nm, respectively. The cross-section image (Figure 2b) displays the compactness of annealed V_2O_5 films [35].

Barreca et al. [36] prepared V_2O_5 thin films by PE-CVD using $VO(hfa)_2{\cdot}H_2O$ (Hhfa = 1,1,1,5,5,5-hexafluoro-2,4-pentanedione) as precursor. This precursor was vaporized at 70 °C at the rate of 2×10^{-4} mmol m^{-2} s^{-1} in a reactor in which argon (constant flow rate ϕ = 40 sccm) and oxygen (flow rate $5 \leq \phi \leq 20$ sccm) were plasma sources. V_2O_5 thin films deposited at T_s = 200 °C and 10 sccm of O_2 are highly textured (14 nm crystallite size) and grow with the (001) preferential orientation. In the metal organic chemical vapor deposition (MOCVD) the organometallic vapor phase takers place at moderate pressure (10–1000 hPa). Watanabe et al. [37] prepared V_2O_5 thin films by means of microwave plasma MOCVD on ITO-coated fused silica substrate. B*is*-

acetylacetonatovanadyl, $VO(acac)_2$, $VO(C_5H_7O_2)_2$ heated at ~600 ℃ was selected as vanadium precursor. Its vapor was injected into the oxygen plasma generated by the microwave discharge. Other experimental conditions were as follows: the substrate was maintained at $T_s \approx 300$ ℃, the O_2 flow was $\phi = 1.2$ dm^3 h^{-1} under pressure of 650 Pa. Typical polycrystalline film, 120 nm thick, was deposited after 15 min. Vanadyl(IV) β-diketonate has been also used with water in a low-pressure reactor under different conditions [38]. A novel vanadium(III) precursor such as vanadium(III) alkoxide [$V(OCMe_2CH_2OMe)_3$] was also used, which presents an appreciable volatility at 55 ℃ under pressure of 200 Pa [39]. Strongly (00*l*)-oriented film composites of V_2O_5–V_6O_{13} were grown at temperatures ≥560 ℃ onto fused quartz substrate using vanadyl acetylacetonate as precursor. Single phase was obtained for substrate maintained at T_s = 580 ℃ due to the reentrant-type growth behavior [40]. V_2O_5 electrochromic films were grown on flexible polymer substrates using plasma-enhanced chemical vapor deposition (PECVD). Films were deposited at high rate of 50 nm min^{-1} from the decomposition of vanadium oxytrichloride ($VOCl_3$) and O_2 [41]. Nandakumar [42] studied the growth rate r_G of CVD V_2O_5 films as a function of T_s and reported an Arrhenius behavior with 0.14 eV activation energy; r_G = 50 nm min^{-1} at $T_s \approx 230$ ℃.

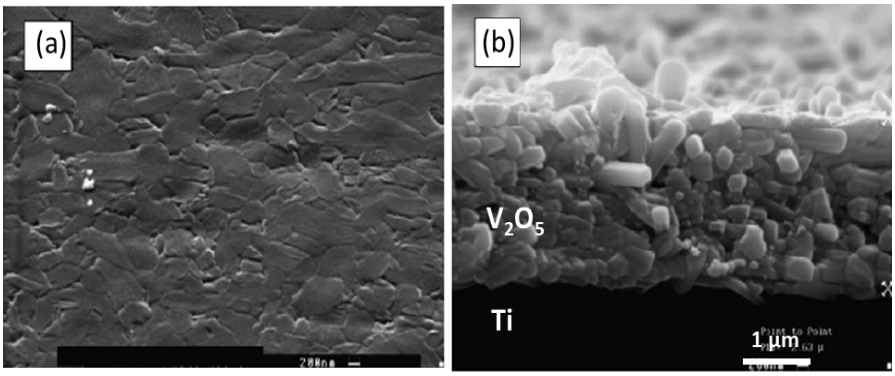

Figure 2. Morphology of CVD V_2O_5 films deposited onto Pt substrate. (a) SEM image of film annealed at 500 ℃ for 2 h and (b) cross section (from Ref. [35]).

2.4. Magnetron sputtering

Sputtering deposition method is the most popular technique to grow metal-oxide films, since it allows faster deposition rates. Its main advantage comes from the production of good surface uniformity of as-deposited films. It includes radio-frequency (r.f.) magnetron sputtering [43–46], direct current (dc) magnetron sputtering [47–49] and ion beam sputtering [50]. The stoichiometry of V_2O_5 films can be tuned by this evaporation method [51,52]. Typical r.f.-magnetron sputtered V_2O_5 films are formed in a plasma sputtering chamber using V_2O_5 target bombarded by argon ions in a plasma of power P_w = 150–300 W. For specific application, low sputtering power P_w < 100 W can be used [53]. The reactive deposition is realized by injection of pure argon and oxygen gases, at flow rate ϕ < 10 sccm. Silversmit et al. [51] obtained V_2O_5 films on Si (100) wafers by reactive dc magnetron sputtering and studied the influence of deposition parameters on their stoichiometry. These experiments were carried out in a vacuum of 5×10^{-5} Pa with a magnetron discharge voltage at ~550 V and a plasma constant current of 150 mA. The O_2 flow was maintained at ϕ = 3.5 sccm. Fateh et al. [54] deposited V_2O_5 films onto (100) oriented Mg substrates and established detailed

synthesis-structure relationships showing the best crystallinity for the film deposited at 80 ℃. Lourenço et al. [55] investigated the effect of different oxygen flow rates on the structure of VO_x films and determined that V_2O_5 films are obtained at high oxygen flows (ϕ > 9 sccm). Benmoussa et al. [56,57] sputtered V_2O_5 thin films on Corning glass and ITO-coated glass substrates for electrochromic application. The films deposited on both substrates are *c*-axis preferred oriented showing that texture is substrate independent.

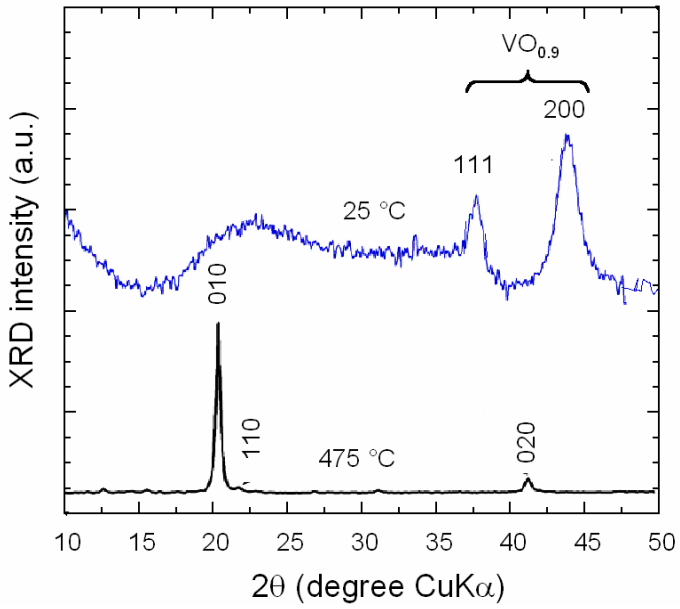

Figure 3. XRD diffractogram for r.f. sputtered V_2O_5 films (a) as-deposited at 25 ℃ and (b) thermally annealed at 475 ℃ in air for 3 h (from Ref. [46]).

Yoon et al. [58] compared the structure of V_2O_5 thin films grown on (100) Si wafers by d.c. and r.f. reactive sputtering at room temperature; d.c.-sputtered films are amorphous, while those prepared from reactive r.f.-sputtering crystallized with large grain size that is due to the self-bias effect. Gianneta et al. [46] deposited VO_x films using a base pressure 1 mPa, a r.f. plasma power of 200 W and an Ar flow ϕ = 20 sccm. As-deposited films are almost amorphous and exhibit broad XRD reflections matching those of $VO_{0.9}$, while annealing at 475 ℃ in air for 3 h promotes the well-crystallized V_2O_5 phase with well-developed orthorhombic shape and grain size >100 nm (see Figure 3). Ottaviano et al. [59] reported the improved electrochromic properties of rf reactive sputtered films deposited at low O_2 flow (2%) showing the highest value of injected charge (49.8 mC cm^{-2}) and the greatest differences in optical density. Lin and Tsai [19,60] prepared V_2O_{5-z} films on flexible PET(polyethylene terephthalate)/ITO (indium tin oxide) substrates. Oxygen deficient V_2O_{5-z} films (z = 0.13) were formed in a chamber pressure of 6 Pa with Ar and O_2 flow rate of 4 sccm that show a transmittance variance od 36.5% after 200 cycles. Kang et al. [61] prepared nanorod-like V_2O_5 film by electron-beam irradiated amorphous film, which were obtained by r.f. sputtering at power of 200 W at 1 nm min^{-1} growth rate on alumina substrate.

2.5. Pulsed-laser deposition (PLD)

Extensive works using the PLD technique have been successful for the growth of V_2O_5 thin films. Advantages include an easily control of the film composition by tuning the deposition parameters and a good reproducible stoichiometry of the target material in the films [62–73]. In the PLD technique, a pulsed laser beam (10 ns duration) is focused by a lens to ablate the V_2O_5 target. The energy of the beam is in the range 100–500 mJ per pulse (laser fluence of 10 J cm^{-2}) with a laser pulse repetition of 10 Hz. Target and substrates are placed inside the deposition chamber evacuated to ~1 mPa. To avoid depletion of deposit at any given spot, the target rotates at 10 rpm. For reactive synthesis, pure oxygen gas is introduced into the chamber with a typical partial pressure (pO_2) in the range 0.1–10 Pa to obtain single-phased and stoichiometric V_2O_5 films. Typical deposition rate is in the range 2–5 Å s^{-1}. Various laser wavelengths are reported in the literature: 532 nm line of a doubled frequency pulsed Nd:YAG laser [63], 248 nm line of a KrF excimer UV laser [62,64] or the 266 nm line of the quadrupled Nd:YAG laser. Zhang et al. [62] prepared PLD crystalline oriented V_2O_5 films deposited at 200 °C in different partial pressure of O_2 + Ar mixed gases. The films grown in oxygen-rich, pO_2 = 0.1 Pa, environment at low substrate temperature $T_s \approx 200$ °C crystallizes in the orthorhombic structure. Iida et al. [65] suggested that films deposited at T_s = 350 °C in a chamber under partial pressure pO_2 = 13.3 Pa using the 238-nm line of a KrF excimer laser have a surface morphology suitable for electrochromic application. The same process was used to grow doped films, with various elements Nb, Ce, Nd, Dy, Sm, Ag [66]. Fang et al. [74] prepared orientated V_2O_5 electrochromic thin films on glass by pulsed excimer laser ablation. Nanocrystalline films highly oriented along the c-axis were obtained at lower temperature T_s (200 °C) that that of thermal vacuum deposition (300–500 °C). McGraw et al. [67] found that the crystallographic texture of PLD V_2O_5 films depends mainly on temperature and oxygen pressure rather than on the choice of substrate. Films deposited on SnO_2/glass substrate are dense and phase pure orthorhombic V_2O_5. For T_s = 200 °C and pO_2 = 2.7 Pa, the films are well (200)-textured, while they are (001) and (101) dual-oriented for T_s = 500 °C and pO_2 > 12 Pa. Ramana et al. [75] investigated the structural patterns of PLD V_2O_5 films which revealed that stoichiometric specimens are well-crystallized with the layered orthorhombic structure even onto amorphous substrates at T_s = 200 °C under partial oxygen atmosphere pO_2 = 10 Pa. Atomic force microscopy (AFM) analysis gave a consistent picture of the surface morphology and microstructure: grains of small size, spherical in shape. Figure 4 shows the variation of the grain size as a function of the growth temperature for various substrate materials. The evolution of the grain size follows an exponential law (dashed lines) as [76]:

$$L_c = L_0 \exp(-Q_d / k_B T) \tag{1}$$

where Q_d is the activation energy, k_B is the Boltzmann constant, T is the absolute temperature, and L_o is a preexponential factor that depends on the physical properties of the substrate-deposit. The grain size appears to be 50–300 nm for films deposited onto glass, 50–400 nm for films on ITO-coated glass and 60–600 nm for films evaporated on Si wafer. Q_d of the PLD V_2O_5 film in the range 0.43–0.55 eV reflects the nucleation rate [64]. AFM images show that films deposited onto Si (8 nm) and ITO-coated glass (10 nm) exhibited lower surface roughness. The dependence of the substrate temperature on the gross microstructure of PLD V_2O_5 films is presented in Figure 5. The domain of optimum controlled morphology is illustrated by the shaded region of substrate temperature range $200 \leq T_s \leq 300$ °C.

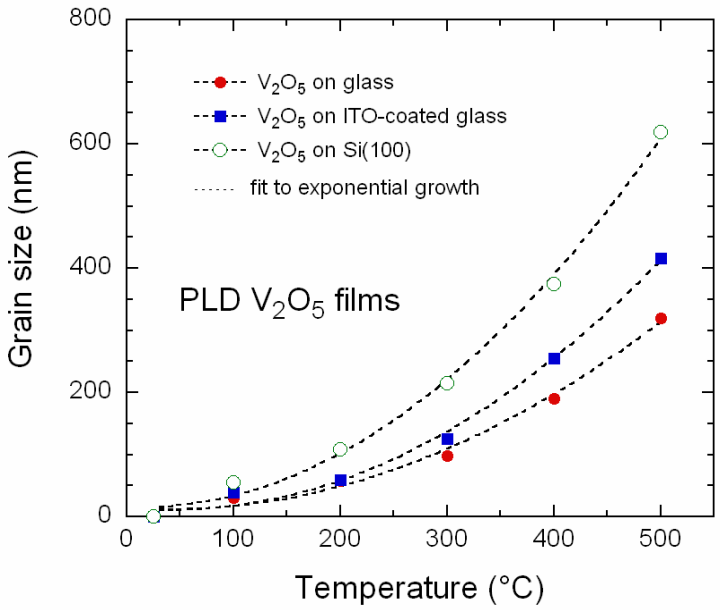

Figure 4. Evolution of the grain size of PLD V_2O_5 films with growth temperature during deposition onto amorphous glass, ITO-coated glass and silicon substrates [64].

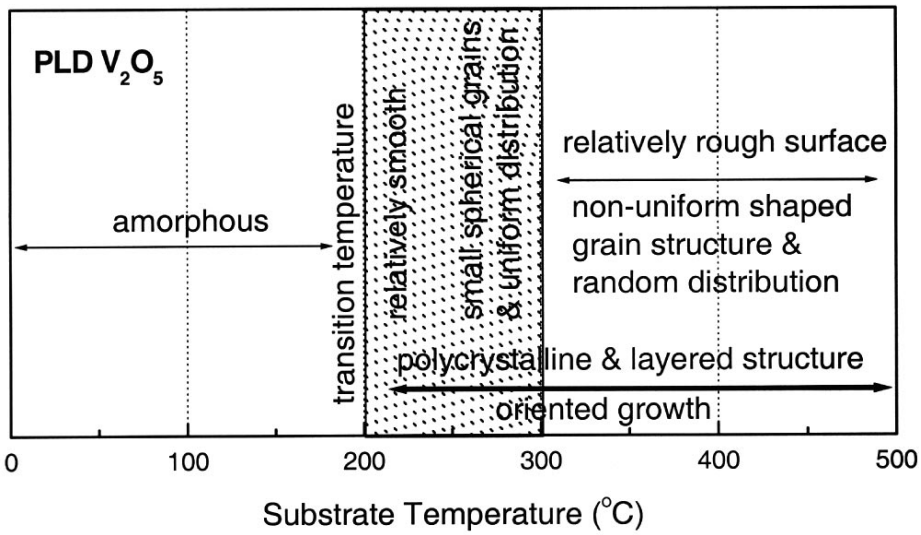

Figure 5. Diagram mapping the effect of substrate temperature on the microstructure evolution of PLD V_2O_5 thin films. The domain of optimum controlled morphology is illustrated by the shaded region of substrate temperature range $200 \leq T_s \leq 300$ °C [76].

2.6. Electron-beam (e-beam) evaporation

The e-beam evaporation method implies a high vacuum coating unit with vacuum better that 0.1 mPa, in which an electron beam accelerated by a voltage of several kV (typically 6 kV) and power density of ~1.5 kW cm^{-2} is scanned on the surface of the target. It is a low-cost technique, which allows high deposition rate (30–50 Å s^{-1}) with good control of the structure and morphology, and allows for sequential and co-deposition with minimum contamination [8,77–84].

In their early work, Ramana et al. [81] reported the growth of non-stoichiometric V_2O_5 films deposited on Corning 7059 glass substrates maintained at T_s = 280 ℃ in a vacuum of 0.05 mPa, while the injection of pure oxygen (partial pressure of 0.1 mPa) produced near-stoichiometric films with pale orange yellow color. The XPS experiments revealed that films formed at room temperature are nearly stoichiometric, while the films formed at elevated temperatures are oxygen deficient. These results are supported by the shift of the vanadyl mode in the FTIR and Raman spectra. However, the films deposited at $T_s \approx 420$ ℃ in oxygen partial pressure of 10^{-4} mbar led to vanadium ions in their highest oxidation state [8,79]. Alumina-doped V_2O_5 thin films, $(V_2O_5)_{100-x}(Al_2O_3)_x$ with x = 5, 10, 15, 20 wt.%, were fabricated by e-beam evaporation method [85]. Thiagarajan et al. [84] studied the physical properties of highly oriented V_2O_5 films (0.8–1.2 μm thick, 31–45 grain size) grown by electron beam evaporation at 200 ℃ throughout all depositions. It was shown that the microstrain decreases with the decrease of the film thickness, due to the reduced dislocation density.

2.7. Spray pyrolysis

Spray pyrolysis is considered as a cost-efficient technique and has been widely employed to fabricate V_2O_5 thin films. Currently, the pyrolysis process is performed at relatively low temperature >500 ℃ [86–90]. The V_2O_5 films are deposited through thermal decomposition of vanadium precursor such as VCl_3 in deionized water [91]. By increasing the spray deposition rates, the crystallite size increases, while the microstrain decreases. Nanostructured flower-like V_2O_5 (crystallite size of ~25 nm) were prepared by spray pyrolysis from 0.1 mol L^{-1} ammonium vanadate in aqueous solution. Polycrystalline films deposited at T_s = 300 ℃ exhibit the largest carrier density 3.6×10^{18} cm^{-3} and the lowest electrical resistivity 5.56 Ω cm^{-1}, which allow to use them as xylene sensors [92]. 10% Mo-doped films (~28 nm crystallite size) prepared by spraying VCl_3 and $MoCl_5$ in aqueous solution on substrate maintained at 380 ℃ crystallize with a tetragonal structure [93]. Wei et al. [90] prepared V_2O_5 films using ultrasonic spray method that revealed a small amount of V^{4+} species. These films heat-treated at 350 ℃ show good charge storage stability over 10000 electrochromic cycles. A d.c. plasma torch was used to atomize the solution $VOCl_3$ precursor, which is injected externally into the plasma flame and deposited on the substrate [88]. Nanostructural V_2O_5 thin films deposited by spray pyrolysis technique exhibit the highest transmittance when deposited at 550 ℃. A shift of the absorption edge from 2.5 to 2.8 eV is observed for T_s > 450 ℃ due to modified chemical bonds at the film/substrate interface [89]. The influence of the molarity of the spray pyrolysis precursor on the structure and morphology of V_2O_5 films shows that vanadium nitrate $V(NO_3)_5 \cdot 5H_2O$ with concentration ≥0.1 mol L^{-1} provides orthorhombic structured films with (001) preferred orientation [94].

2.8. Sol-gel

Sol-gel method is a low-temperature wet-chemistry method in which the raw materials are mixed at the molecular level. Wang et al. [95] investigated the structural modifications of spray deposited $V_2O_5 \cdot nH_2O$ xerogel films as a function of post-annealing temperatures. Films sprayed at 150 ℃ showed broad peaks in their ^{51}V NMR spectra for heat-treatment at $T_a \approx 120$ ℃, which gives evidence of a distortion of the square pyramids. The structural feature of $V_2O_5 \cdot nH_2O$ (with structural water) favors the lithium intercalation between the slabs with respect to contracted dried films at

T_a > 250 ℃. The effect of deposition conditions and post-annealing treatment of xerogel V_2O_5 films was studied by several groups. Najdoski et al. [96] examined the electrochromic properties of $(NH_4)_{0.3}V_2O_5 \cdot 1.25H_2O$ nanostructured films deposited onto SnO_2:F (FTO) as a function of the temperature of preparation. Elongated aggregates 250–500 nm length were obtained at 50 ℃, while shorter particles (50–300 nm) were obtained at 85 ℃. Chen et al. [97] prepared thin films by spin coating of the sol-gel composed by the mixture of V_2O_5 powders benzyl alcohol (BA) and isobutanol (IB) (molar ratio 1:40:4) heated at 110 ℃ for 5 h. Wang et al. [98] fabricated $V_2O_5 \cdot nH_2O$ xerogel films by reacting V_2O_5 and H_2O_2 under ambient conditions. $V_2O_5 \cdot \frac{1}{3}H_2O$ film exhibited the best Li^+ intercalation properties with a stabilized specific capacity of 185 mAh g^{-1} at 0.1 mA cm^{-2} current density after 50 cycles. Cazzanelli et al. [99] analyzed the Raman spectra of xerogel films intercalated with lithium. $V_2O_5 \cdot nH_2O$ xerogel films ($1.8 \leq n \leq 0$) were spin-coated at angular velocity of 1500 rpm. Spectral features of Li-intercalated samples show significant effect of the water content in the interlayer space inducing new Raman bands at 800 and 950 cm^{-1}. V_2O_5 films deposited by the doctor-blade route using polyol dispersed in waterand acetyl acetone crystallized with the *C*2/*c* structure, which transformed to orthorhombic *Pmmn* (86 nm crystallite size) after calcination at 170 ℃ for 3 h [22]. Dip-coating method was used to produce V_2O_5 xerogel films from organic (vanadium tri-isopropoxide into isopropyl alcohol) and inorganic (V_2O_5 powers in 15 wt.% H_2O_2) precursors [100,101]

2.9. Electrodeposition

A typical electrodeposition experiment takes place in an aqueous solution of vanadium precursor such as vanadyl sulfate hydrate ($VOSO_4 \cdot nH_2O$) or V_2O_5 powers dissolved in hydrogen peroxide as electrolyte using a constant potential (1.7 V vs. Ag/AgCl) [18,102,103]. Liu et al. [104] prepared nanostructured V_2O_5 films by means of cathodic deposition from V_2O_5 and H_2O_2 aqueous solution. As-deposited samples contained 14% V^{4+}, while annealing at 500 ℃ in air oxidized all vanadium cations. Electrochromic V_2O_5 films were synthesized by electrophoretic deposition of a sol formed by the dissolution of V_2O_5 powers in H_2O_2 solution with the H_2O_2/V_2O_5 ratio of 8:1. The deposition occurred in a Teflon vessel at the voltage of 5 V using a Pt rod as counter electrode [102]. The electrodeposition experiments carried out by Vernardou et al. [18] consisted in the coating of V_2O_5 powders dissolved in a solution of methanol and water as electrolyte to form an orange suspension. Pt rod was the counter electrode. Experiments were performed using deposition current density of 0.25 mA cm^{-2}.

2.10. Atomic layer deposition (ALD)

The atomic layer chemical vapor deposition (ALCVD) was successfully applied to grow V_2O_5 films [105–112]. This method provides uniform and compact films with a high control of phase formation and the film thickness that include atomic layer epitaxy (ALE) and atomic layer deposition (ALD). ALD process consists in alternative exposition of a substrate to the precursor fluxes, which are timely separated in space. In principle this process is self-limiting as the monomolecular layers are absorbed with molecular excess flushed away by evacuation of the system. The vapor pressure of the precursor must agree with the deposition temperature chosen. Groult et al. [105,106] prepared nanometric V_2O_5 thin films deposited onto Si wafers (100) by means of ALCVD.

The atomic layer deposition (ALD) technique is proven suitable for the growth of uniform and pin-hole free V_2O_5 thin films. ALD is becoming an attractive process to prepare thin films for energy storage, because it allows the control of deposit films of thickness in the range 1–100 nm with remarkable uniformity and control of the thickness. V_2O_5 has been synthesized by this process by several authors [113–119]. This scalable method, which allows to do bath processes, is based on self-limited reactions between gas phase precursors and active sites on surfaces. This technique leads to monolayer thickness control. The growth of V_2O_5 thin films consists of the successive cycles of deposition of atomic layers from the reaction of a vanadium precursor with oxygen. Various vanadium precursors have been proposed such as vanadyl tri-isopropoxide $VO(OC_3H_7)_3$ ($VO(OPr^i)_3$, VTIP), vanadyl triethoxide ($VO(OEt)_3$), vanadyl triisobutoxide ($VO(OBui)_3$), vanadyl acetylacetonate ($VO(acac)_2$) and vanadium acetylacetonate ($V(acac)_3$ (acac = $C_5H_7O_2^-$)), VTIP being the most popular due to its high vapor pressure (38 Pa at 45 °C) and its rapid reaction with water [107–109]. Examination of the literature shows that the choice of ALD precursors has a significant impact on the crystallinity and morphology of V_2O_5 films. One ALD cycle is composed of four pulses in the sequence $t_1/t_2/t_3/t_4$, where t_i is the duration (in s) of injection of V precursor, purge, reactive gas, purge, respectively. For instance, the global ALD reaction of VTIP precursor with water is:

$$VO(OC_3H_7)_3 + 3H_2O \rightarrow V_2O_5 + 6HOC_3H_7 \quad (2)$$

The pressure of (VTIP) in the reactor is adjusted to 5 mPa and the water pressure to 0.3 Pa. Typical cycle to grow V_2O_5 films lasts 17 s (2 s VTIP, 5 s pumping, 5 s reactive gas and 5 second pumping) that makes a growth rate of 0.7 Å per cycle. Several authors demonstrated that the rate-determining step is the oxidant in O_3-based or H_2O-based ALD reaction [109,110]. Keränen et al. [107] prepared ALD V_2O_5 films deposited onto various metal oxides for catalytic applications using $VO(acac)_2$ as V precursor with a N_2 flow of 3 $dm^3\ h^{-1}$. Chen et al. [111] used a water-free system to prepare crystalline as-deposited V_2O_5 films from VTIP and ozone, using an Al_2O_3 template at low temperature (170–180 °C). With this process, a deposition rate of 0.27 Å per cycle onto Si wafer was achieved. Badot et al. [110] reported a growth rate of ~20 ng cm^{-2} per cycle at 170 °C using VTIP + water sequence. With these growth conditions and annealing at 400 °C, the ALD V_2O_5 films were well-crystallized and preferentially oriented with the (*a,b*) planes parallel to the SnO_2-coated glass substrate. ALD V_2O_5 films deposited onto Ti foil using the VTIP-water vapor route in the pulsing sequence—VTIP/N_2 purge/H_2O vapor/N_2 purge of 200/400/2400/1000 ms and annealed at 500 °C for 2 h showed a small-polaron drift mobility of 1.84×10^{-2} $cm^2\ V^{-1}\ s^{-1}$ at room temperature (activation energy of 0.14 eV) [112]. Ostreng et al. [113] prepared nano-structured ALD V_2O_5 films from vanadyl 2,2,6,6-tetramethylhepta-3,5-dione ($VO(thd)_2$) and ozone at 215 °C with N_2 as carrier gas (500 sccm flow) applied as cathode films for lithium microbatteries. 86-nm thick films oriented along a (001)/(010) orientation were thus obtained after 2000 cycles. Chen et al. [114] employed VTIP precursor with both O_3 and H_2O as oxidant. For ALD cycles operating in the 170–185 °C window, the water-VTIP route (growth rate 0.4 Å per cycle) produces amorphous films, while crystalline films are formed with the ozone-VTIP reaction (growth rate 0.20 Å). The transition from amorphous to crystalline structure was characterized by rectangular V_2O_5 nanograins (20 nm size) with a monomodal distribution starting at 400 °C.

A comparison of thermal and plasma-enhanced ALD/CVD has been carried out by Musschoot et al. [109]. Chen et al. [114] determined that areal energy and power density is optimized

with V_2O_5 thickness round 60 nm. Larger thickness results in a decrease of the rate capability due to the small intrinsic diffusion coefficient of lithium, while thinner films suffer from a decrease of material loading. The authors estimated that the device would outperform the gravimetric power density of the current Li-ion batteries by one order of magnitude. Song et al. [114] adopted to deposit V_2O_5 thin films by ALD using vanadyl tri-isopropoxide and water and showed remarkable electrochemical response and voltage-induced insulator-to-metal transition. Ultrathin V_2O_5 films (10–90 nm thick) were prepared by ALD using vanadyl acetylacetonate as the vanadium precursor [119]. Crystalline films were obtained below 200 ℃ yielding a growth rate of 4.5 pm per cycle. Heterojunction diodes based on TiO_2(p)-(n)V_2O_5 were fabricated as humidity sensor.

3. Characterizations of V_2O_5 films

3.1. Structure and morphology

V_2O_5 is the highest oxidation compound of the vanadium oxide system which crystallizes with a lamellar orthorhombic structure in space group *Pmmn* (D_{2h}^{13}, No. 59) with lattice parameters a = 11.512 Å, b = 3.564 Å, c = 4.368 Å and V = 179.17 Å^3 (see Table 1). It has a layered structure with atomic layers in the [100] × [010] plane and van der Waals-type interlayer coupling. The structure is formed of three types of oxygen atoms: apical-vanadyl (O_{van}), bridge (O_{bri}) and chain (O_{ch}) (see Figure 6). Oxygen vacancies in $V_2O_{5-\delta}$ are predominantly of the O_{van} type, forming the vanadyl bonds. Atomic positions in V_2O_5 are summarized in Table 1. Pure V_2O_5 is a diamagnetic semiconductor with an energy gap (E_g) of 2.2–2.3 eV [120], while oxygen-deficient material is ferromagnetic with spin moment ~2 μ_B per vacancy [121]. A density functional calcualtion of the electronic structure is given in Refs. [122,123]. The role of octahedral deformations has been explored in [124].

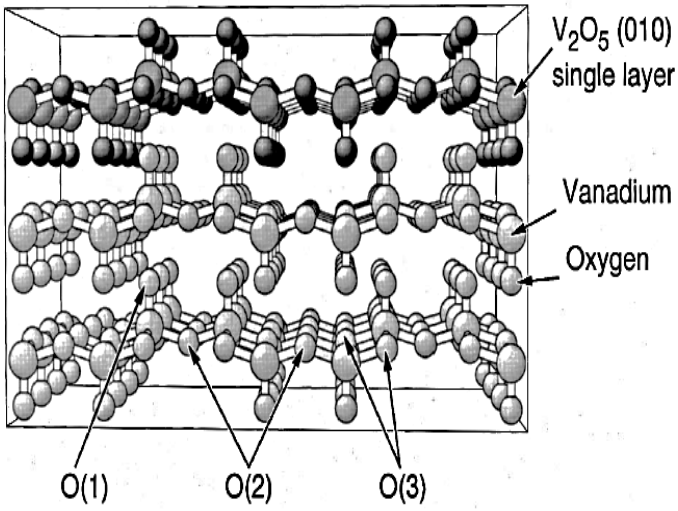

Figure 6. Structure of orthorhombic V_2O_5 with netplane stacking along the (010) direction that shows the vanadium and inequivalent oxygen singly coordinated apical vanadyl-O_{van}, doubly coordinated bridge-O_{bri}, and triply coordinated chain-O_{ch} atoms (from Ref. [123]).

Table 1. Atomic positions in orthorhombic V_2O_5 (space group *Pmmn*) (from Ref. [124]).

Atom	Wyckoff position	Parameters		
		x	y	z
V	4f	0.10118	0.25	−0.1083
O_{van}	4f	0.10430	0.25	−0.469
O_{br}	2a	0.25	0.25	0.001
O_{ch}	4f	−0.0689	0.25	0.003

Figure 7 shows the typical XRD patterns of V_2O_5 films deposited by PLD (a) and (b) by electron beam (EBD) techniques. The spectra of samples deposited at low T_s are rather amorphous, while they can be obtained crystallized by raising the substrate temperature and/or increasing $p(O_2)$. The significant feature is the growth of XRD reflections at ca. $2\theta = 20.26°$ and around $2\theta = 41.4°$ that correspond to the (001) and (002) lattice planes of the orthorhombic structure, respectively. The (001) reflection is the dominant line for well-crystallized films showing the preferential *c*-axis orientation lying perpendicular to the substrate with stacking *ab* planes [125]. Gradual increase in intensity of the (101) reflection at high T_s is attributed to a re-organization process of the in-plane V–O–V chains in flash-evaporated film. This crystallographic behavior seems to be the general trend for the growth of V_2O_5 films; it has been found for various deposition techniques: as-prepared r.f. sputtered films under a gas mixture of Ar and O_2 [56,126], sol-gel spin-coated films annealed at 400 °C [127], pulsed-laser deposited V_2O_5 films [63], plasma-enhanced CVD method [128] and vapor deposition in high vacuum [26,129] on heated substrates. The c-axis preferred growth was also found for films prepared by ALD [110,113] and EBD [79] processes. Well-ordered V_2O_5-(001) films were obtained by the oxidation of vacuum deposited vanadium layers with oxygen partial pressure of 50 hPa [130]. Due to the imperfect stacking of ab planes built up of O_{van}, the (001) orientation for crystalline V_2O_5 films deposited by PECVD from a vanadyl(IV) β-diketonate compound appears at T_s as low as 150 °C [38], while higher temperature $T_s = 240$ °C for films prepared by CVD of $VOCl_3$ with water [131]. Note that films prepared from sol-gel precursor display complex behavior due to the large fraction of water content. For instance, the XRD spectrum of spin-coated films obtained from $V_2O_5 + H_2O_2$ sol-gel (crystallized at $T_a = 150$ °C) displayed the dominant (110) Bragg line, which disappeared and was replaced at $T_a = 300$ °C by the (00*l*) reflections showing the nucleation parallel to the substrate [121]. Other workers found that spin-coated films crystallize above 350 °C [132]. The texture of V_2O_5 films grown by ALD technique varies with the number of deposition cycles (n_c). For $n_c < 1000$, the predominant orientation is along the (001) plane, which is modified for $n_c \approx 2000$ with the appearance of sharp (0k0) Bragg reflections. Finally (021) and (061) reflections are observed for $n_c \approx 5000$. This is attributed to the overgrowth of nuclei on the surface of platelets with their edges orientated normal to the substrate [113]. Similar thickness (d_f) effect was observed on e-beam deposited films [84]. Moreover, the increase of the peak broadening of the (001) lattice place with d_f is attributed to microstrains inversely proportional to the crystallite size that linearly decreases with the increase in d_f.

Rajendra-Kumar et al. [133] deposited V_2O_5 films at various substrate temperatures ($25 \leq T_s \leq 400$ °C) using vacuum evaporation technique. The orthorhombic lattice parameters "*a*" and "*c*" of polycrystalline films determined by Nelson-Rieley function were found to decrease when the deposition temperature increases (Figure 7a). According to the model proposed by Gilles and

Boesman [134] from EPR spectroscopy, these structural changes are assigned to the increase of non-stoichiometry (oxygen vacancies) leading to a contraction of the (001) interplanar spacing.

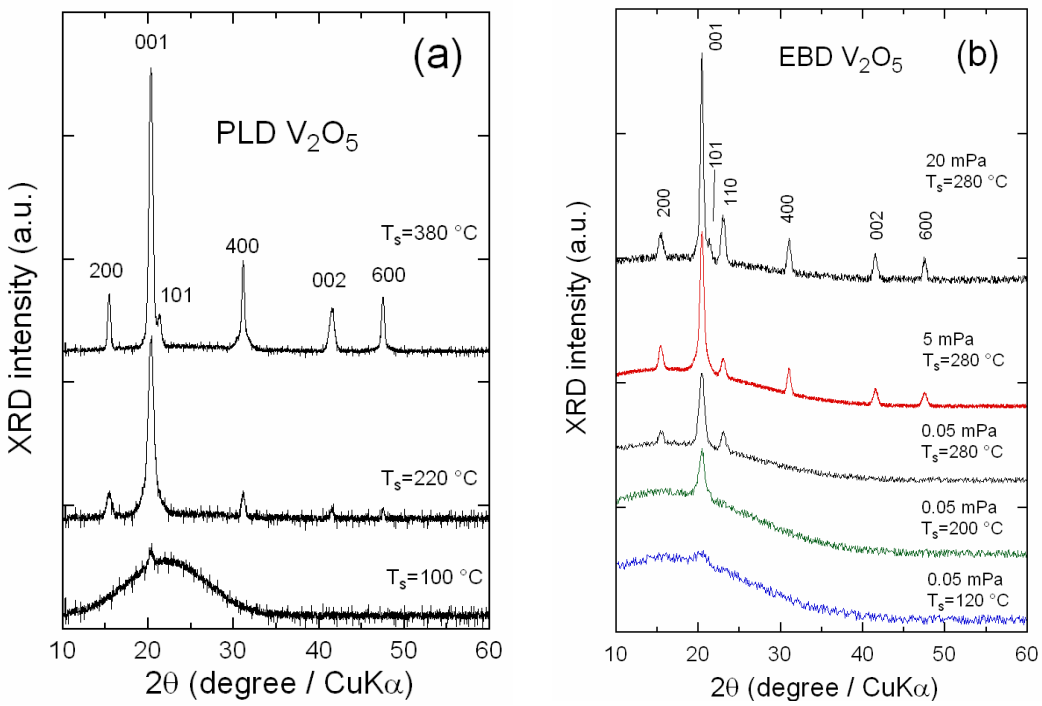

Figure 7. XRD patterns ox deposited V_2O_5 films. (a) PLD films grown at various substrate temperatures [75]. (b) EBD films grown using various oxygen partial pressures [79].

The crystallite size L_c of composites is calculated using the Scherrer's formula by considering the (002) reflection line:

$$L_c = \frac{K\lambda}{B\cos\theta} \tag{3}$$

where K is the shape factor, which varies with the crystallite shape (0.89 for spherical crystallites), λ is the wavelength of X-ray radiation (0.15406 nm), B is the full-width at half maximum (FWHM) expressed in radians and θ is the Bragg angle. Generally, the peak intensity and the full-width at half-maximum (FWHM) vary with the deposition conditions, which indicates differences in crystallinity, particle sizes and ordering of local structure between samples. The analysis is obtained by the combination of the Scherrer and Bragg formulæ:

$$B^2\cos^2\theta = 16e^2\sin^2\theta + \frac{K^2\lambda^2}{L_c^2} \tag{4}$$

where $\langle e^2\rangle$ denotes local strain (defined as $\Delta d/d$ with d the interplanar spacing). From the slope $16\langle e^2\rangle$ and intercept $K^2\lambda^2/L_c^2$ of the plot of $B^2\cos^2\theta$ as a function of $\sin^2\theta$, one can estimate the strain $\langle e^2\rangle$ and coherence length L_c. The variation of the local strain as a function of the substrate temperature for V_2O_5 films deposited by PLD method is reported in Figure 7b.

The surface morphology and surface topography are currently investigated by scanning electron microscopy (SEM) and atomic force microscopy (AFM) as a function of at various T_s. The AFM images recorded at the scan area of 2 × 2 μm^2 for thermally evaporated V_2O_5 films are displayed in Figure 8 [82]. These patterns show that both the surface roughness and the grain size increase with the increase in T_s. Surface roughness of 27 nm and grain size of 130 nm are found for films deposited at 300 ℃. It was demonstrated that the morphology, structure and optical and electrical properties of dip-coated V_2O_5 films are affected by the sol aging [135–138]. Senapati and Panda [131] investigated nanoscale films prepared by spin coating of $V_2O_5{\cdot}nH_2O$ sol at different stages of aging. Microstrains of films 92–137 nm thick were found to decrease from 4.93 × 10^{-3} for fresh sol to 2.62 × 10^{-3} for 192 h for aged sol in relation to the water loss, while the optical bandgaps decrease from 2.66 to 2.36 eV suggesting a decrease in the localized states with aging.

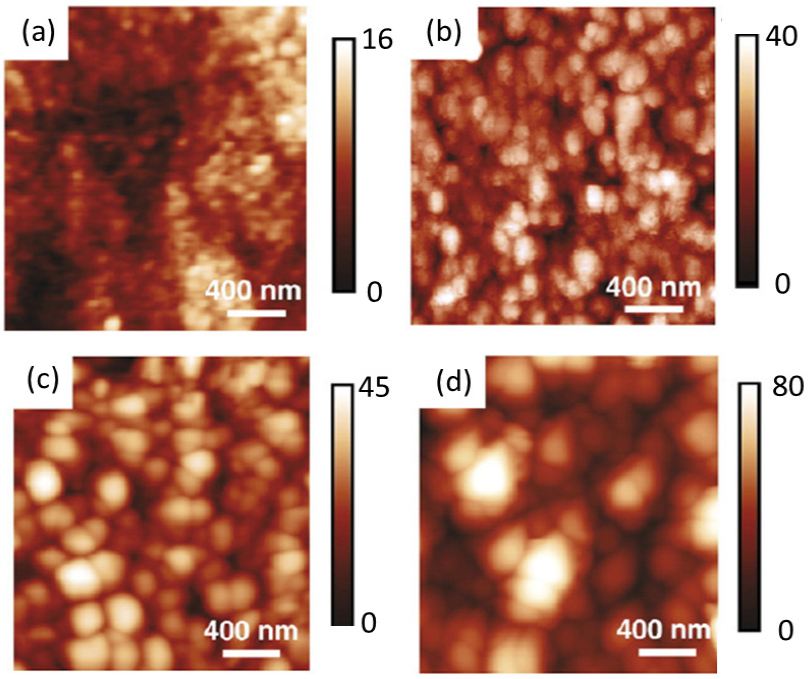

Figure 8. AFM images of the V_2O_5 films at various T_s: (a) T_s = 25 ℃, (b) post-annealed film deposited at 25 ℃, (c) T_s = 300 ℃ and (d) T_s = 500 ℃ (from Kumar et al. [82]).

3.2. Optical properties

Optical properties of V_2O_5 thin films were investigated by means of absorption measurements for the determination of the optical bandgap, dispersion parameters and spectral window of electrochromic films. Optical absorption coefficient α is calculated by the relation:

$$T = \frac{(1-R)^2 \exp(-\alpha d)}{1-R^2 \exp(-2\alpha d)} \tag{5}$$

where T and R are the spectral transmittance and reflectance and d the film thickness. The interference effect due to internal reflection at normal incidence is negligible for higher optical density ($\alpha d > 1$) that reduce Eq 1 to:

$$T \approx \exp(-\alpha d) \tag{6}$$

and the optical absorption coefficient becomes:

$$\alpha = -(1/d)\ln(T) \tag{7}$$

The optical bandgap E_g^{opt} of a semiconductor is calculated using the interband absorption theory:

$$\alpha h\nu_i = A(h\nu_i - E_g^{opt})^n \tag{8}$$

where ν_i is the incident photon energy, A is a probability parameter and n is the transition coefficient with $n = 2$ for indirect transition and $n = 3/2$ for direct bandgap that is the case of V_2O_5.

Overall, optical absorption spectra, electrical conductivity and electron paramagnetic resonance (EPR) spectra of V_2O_5 show a polaronic character. The polaron originates from the oxygen vacancies that result in an excess of electrons localized in the empty 3*d* orbitals of vanadium atoms. Consequently, V^{5+}/V^{4+} pairs are closed to oxygen vacancies and result in an absorption in the infrared spectrum. The optical transmittance T_{opt} of V_2O_5 prepared by e-beam deposition at different oxygen partial pressure revealed a sharp increase of T_{opt} in the spectral range 550–600 nm. This is due to the fundamental absorption edge that shifts towards the higher energy with the increase in oxygen partial pressure. Figure 9 shows the plots of $(\alpha h\nu_i)^{2/3}$ vs. photon energy for V_2O_5 deposited at T_s = 280 °C under various oxygen partial pressure. The high value of the optical bandgap E_g = 2.32 eV determined by extrapolation of the linear part of the graph to zero (α = 0) indicates that the films are stoichiometric for $p(O_2)$ = 20 mPa, while oxygen vacancies are created at lower pressure.

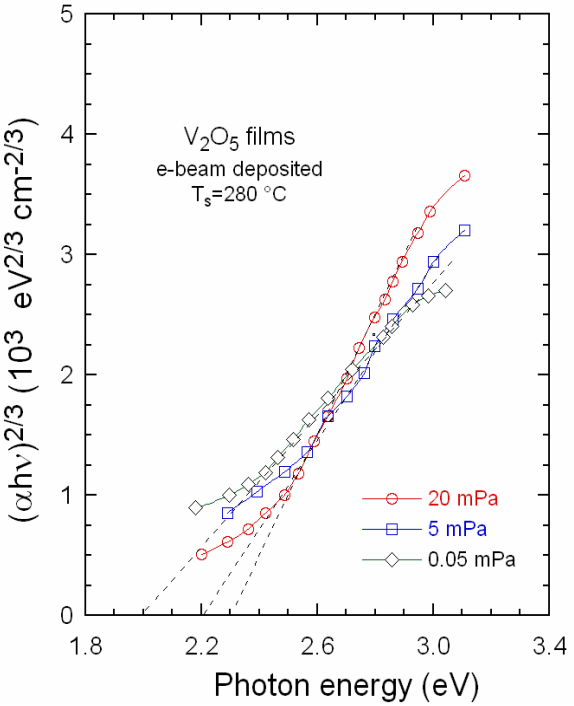

Figure 9. Tauc plots of $(\alpha h\nu_i)^{2/3}$ vs. photon energy for V_2O_5 e-beam deposited at T_s = 280 °C under various oxygen partial pressures (from Ref. [81]).

The partial filling of oxygen vacancies results in a decrease of the concentration of electronic localized states and an increase of E_g. The overall process of oxygen loss can be expression by the Kroger notation:

$$\begin{aligned} O_o^x &\leftrightarrow V_o^x + \frac{1}{2}O_2 \\ V_o^x &\leftrightarrow V_o^{\bullet} + e' \leftrightarrow V_o^{\bullet\bullet} + 2e' \end{aligned} \tag{9}$$

Lourenço et al. [55] studied the effect of oxygen flow rate ϕ on the optical properties of r.f. sputtered V_2O_5 films. The highest E_g = 2.56 eV was obtained at low ϕ = 1 sccm while higher ϕ produced films with an optical bandgap in the range 2.41–2.45 eV. Optical bandgap data of the literature for r.f. sputtered films are in the range 2.15–2.40 eV [56,139,140]. The evolutions of both the width of electronic localized states E_{els} and the bandgap E_g as a function of T_s and as a function of $p(O_2)$ for e-beam evaporated V_2O_5 films are shown in Figure 10a,b respectively. These results show that stoichiometric films were obtained at $p(O_2) > 5$ mPa and $T_s < 100$ °C [79].

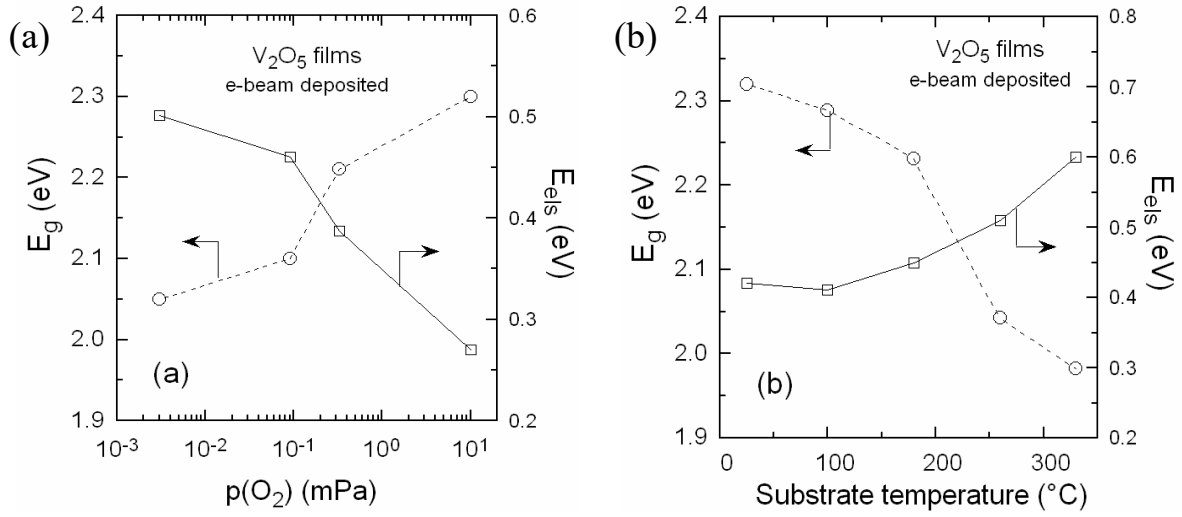

Figure 10. Evolution of both the width of electronic localized states E_{els} and the bandgap E_g as a function of T_s and as a function of (a) $p(O_2)$ and (b) T_s for e-beam evaporated V_2O_5 films (from Ref. [81]).

Song et al. [141] determined the work function of the annealed V_2O_5 films synthesized by VTOP-based ALD method at 135 °C using valence-band ultraviolet photoelectron spectroscopy (UPS). The results showed that the valence band maximum (E_v) is located at ~2.45 eV below the Fermi level (E_F) and gave evidence of an indirect bandgap (E_g) of ~2.63 eV for V_2O_5 film annealed at 500 °C for 1 h in air. Irani et al. [89] investigated the structural and optical properties of nanostructured V_2O_5 thin films deposited by spray pyrolysis technique. The substrate temperature T_s appears to be the key growth along the (001) direction with an orthorhombic structure. It was pointed out that crystallites increased with elevating T_s, reached a maximum at T_s = 450 °C and decreased for T_s > 450 °C. Optical characterizations showed that the highest transmittance occurs for T_s = 550 °C and the absorption edge shifts from 2.5 to 2.8 eV due to the formation of chemical bonds at the interface between V_2O_5 film and substrate.

Beke et al. [73] determined a bandgap of 2.52 eV for PLD V_2O_5 films prepared onto amorphous glass substrate with $p(O_2)$ = 13.3 Pa and T_s = 220 °C but did not distinguish between indirect allowed (n = 1/2) and direct forbidden (n = 3/2) transitions. Luo et al. [142] reported the indirect allowed transition (n = 2) that leads a decrease of E_g from 2.29 to 2.02 eV with increasing T_s from 275 to 320 °C for d.c. magnetron sputtered films. Similar trends were obtained on PVD films [143]. Ramana et al. [72] investigated the effect of the grain size on the optical properties of PLD films. The increase of grain size from 0 to 300 nm produces a red shift of the absorption edge (decrease of E_g) from 2.47 to 2.12 eV following a parabolic behavior that is attributed to the imperfections at grain-boundary regions. The optical absorption was explored on e-beam deposited V_2O_5 films grown at 200 °C on glass substrate with various thicknesses (~0.8–1.2 μm) [84]. The authors elucidated the role of film thickness; the indirect optical bandgap E_g = 2.36 eV is found for thicker films. Optical constants of V_2O_5 films, i.e., refractive index n_{opt}, extinction coefficient k, and plasma frequency ω_p have been investigated by Akl [144]. Determination of the optical bandgap of 2.25 eV was obtained after roughness correction for d.c. magnetron reactive-sputtered α-V_2O_5 films after heating at 500 °C for 1 h in oxygen atmosphere [145]. Ellipsometry measurements were performed as a function of incident angles on (001) oriented sputtered films yield the values of the refractive index n = 2.67, optical absorption coefficient k = 0.0011 and thickness d = 165 nm [146].

3.3. X-ray photoelectron spectroscopy

X-ray photoelectron spectroscopy (XPS) is the common technique to investigate the composition of the V_2O_5 surface and the oxidation states of elements [79,97,147–150]. The typical V 2p and O 1s XPS spectra recorded in the energy range of 510–540 eV for V_2O_5 thin films deposited by EBD technique at various T_s are displayed in Figure 11. The clear evolution of the spectral response corresponds to the V/O ratio in VO_x lattices. Analysis of the XPS spectrum of a V_2O_5 film deposited at T_s = 400 °C under oxidizing atmosphere $p(O_2)$ = 0.01 mPa is presented in Figure 12. The binding energies of the V 2p levels are 516.9 and 524.5 eV for V $2p_{3/2}$ and V $2p_{1/2}$, respectively, with a splitting of 7.6 eV, whereas the binding energy of the O 1s level is 529.6 eV. For more detailed information, the background corrected spectrum was fitted by Gaussian profiles. Different V 2p and O 1s components are detected upon deconvolution by the fit by six Gaussian functions at binding energies of 514.8, 516.9, 520.8, 524.2, 529.7 and 532.5 eV that correspond to V^{4+} $2p_{3/2}$, V^{5+} $2p_{3/2}$, O 1s' satellite of O^{2-}, V^{5+} $2p_{1/2}$, O 1s of O^{2-}, and O^{-}, respectively, as shown in Figure 12. From these results, the relative amounts of ions in different chemical states could be calculated by taking into account the atomic sensitivity factors: 1.41 for V $2p_{3/2}$ and 0.63 for O 1s. Note that the energy splitting between V $2p_{3/2}$ and V $2p_{1/2}$ levels is Δ = 7.3 eV for stoichiometric $VO_{2.5}$ film.

The chemical composition and topography of V_2O_5 thin films at different steps of Li insertion/de-insertion have been investigated by quantitative XPS and AFM analyses [151–154]. From the first cycle, a solid electrolyte interface (SEI) layer has grown on the whole electrode surface, which consists of Li_2CO_3 aggregates. XPS analysis shows that various chemistries appeared during the cycle of charge/discharge such as partial dissolution of the initial Li_2CO_3 layer, residual deposit of ROLi (R = radical), PEO and oxalates. The overall dissolution/residue deposit process explains the capacity loss noticed at the end of the first cycle. Time flight secondary ion mass

spectroscopy (ToF-SIMS) was carried out to analysize the ion distribution in V_2O_5 thin films [150,155].

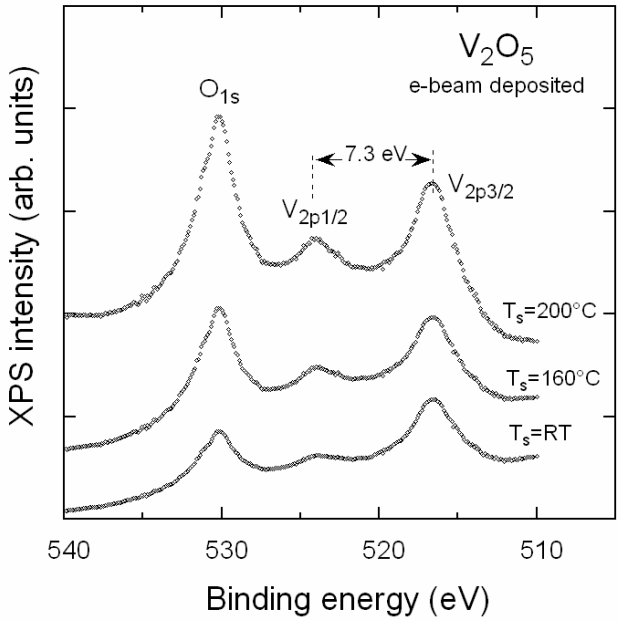

Figure 11. XPS spectra of V_2O_5 films prepared by e-beam deposition for various substrate temperatures $25 \leq T_s \leq 200$ °C.

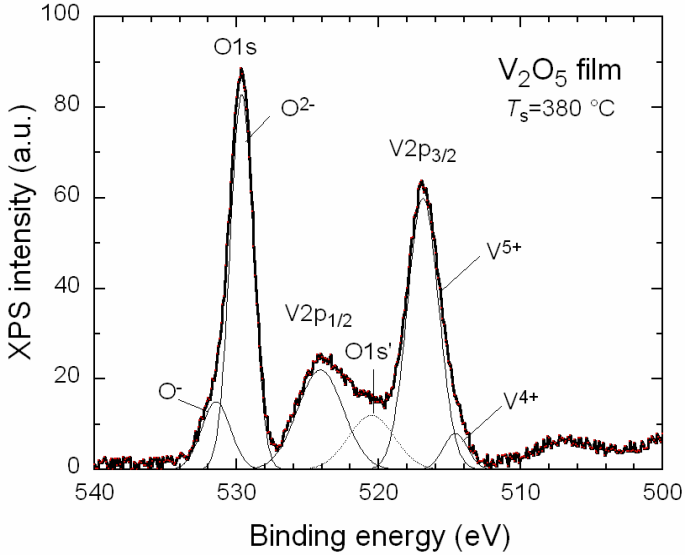

Figure 12. Analysis of the XPS spectrum of a V_2O_5 film deposited at T_s = 400 °C under oxidizing atmosphere $p(O_2)$ = 0.01 mPa.

3.4. Vibrational spectroscopy

Among the local probes, Raman scattering (RS) and Fourier transform infrared (FTIR) spectroscopy are techniques sensitive to the short-range environment of oxygen coordination around

the cations [156]. As a first approximation, the spectra consist of a superposition of the components of all local entities present in the same material in contrast to diffraction data, which give a weighted average. As a rule, the frequency and relative intensity of the bands are sensitive to coordination geometry and oxidation states [157]. Both FTIR and RS spectroscopies are also probing the stoichiometry of films (Figure 13). The vibrational spectra of V_2O_5, which crystallizes in the orthorhombic system (*Pmmn* space group) with D_{2h}^{13} spectroscopic symmetry, are composed of internal modes of the V_2O_5 layer in the *ab* crystal plane and the external mode in the low-frequency region (~144 cm^{-1}) [158]. V_2O_5 has the spectroscopic D_{13}^{2h} symmetry with the Wyckoff 4*f* position for the vanadium, vanadyl and chain oxygen atoms whereas the bridge oxygen occupies the Wyckoff 2*a* position [124]. The vibration modes associated to the D_{2h} factor group decomposed as: $\Gamma_{opt} = 7A_g + 7B_{1g} + 3B_{2g} + 4A_{3g} + 3A_u + 3B_{1u} + 6B_{2u} + 6B_{3u}$. According this decomposition, 21 modes of vibration are Raman active ($7A_g + 7B_{1g} + 3B_{2g} + 4A_{3g}$) and 18 modes are infrared active ($3A_u + 3B_{1u} + 6B_{2u} + 6B_{3u}$) [158,159].

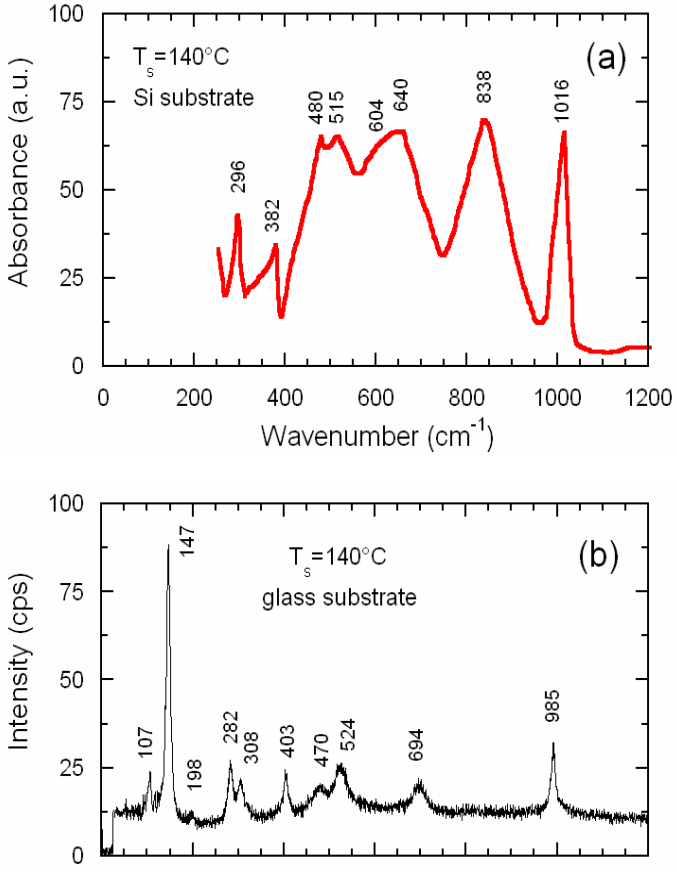

Figure 13. Vibrational spectra of V_2O_5 crystalline films prepared by pulse laser deposition. (a) FTIR spectrum of film deposited onto Si wafer. (b) Raman spectrum of film deposited onto glass substrate.

Ex situ and *in situ* FTIR spectra of V_2O_5 crystalline films prepared by dip-coating from V-oxoisopropoxide sols have been investigated as a function of the degree of Li^+ intercalation and analyzed in terms of dispersion analysis (LO and TO phonons) [160]. A diagnostic test to

differentiate the safe region upon intercalation has been established by the red-shift of the V–O_A stretching frequency at 1016 cm^{-1} and the disappearance of the bridging V–O_B–V stretching mode at 795 cm^{-1}.

Numerous studies of the Raman spectroscopy of V_2O_5 films have been performed on as-deposited, heat-treated, and Li-intercalated samples [9,99,161]. The typical Raman spectrum exhibits more or less well-defined internal and external modes, indicative of the film purity and crystallization (Figure 13b). The internal modes (in the high-frequency region) are the V=O bending vibration at 283 and 405 cm^{-1} and the bending vibration of the bridging V–O–V bonds at 485 cm^{-1}, the V–O stretching mode at 525 cm^{-1} that results from the corner-shared oxygen atoms, and the vanadyl terminal oxygen stretching mode at 993 cm^{-1}. The external modes are generated by the motions of two V_2O_5 layers of the elementary unit cell; these translational vibrations occur at 144 and 196 cm^{-1} (skeleton vibrational modes) [71,76]. The RS spectra of V_2O_5 films deposited by flash-evaporation onto silicon substrate show frequency shift of the vanadyl mode at 995 cm^{-1} (due to the shortest (1.58 Å) V=O double chemical bond stoichiometry) in relation with the stoichiometry of the film [9,161]. Ramana et al. [71] reported a frequency shift of the vanadyl vibration at 993 cm^{-1} with the substrate temperature for V_2O_5 films prepared by PLD technique at $200 \leq T_s \leq 500$ °C, which is attributed to the stress developed in the film. As XRD patterns indicate that the films deposited at $T_s > 200$ °C are polycrystalline with a preferred orientation along the c-axis, the shift of the vanadyl mode suggests a structural organization that introduces a stress associated to a compression in the layered structure. Raman spectroscopy was utilized to characterize the microstructure of V_2O_5 films prepared by d.c. magnetron sputtering on Si (111) wafer. Optimized films with a mere desirable layer-like lattice were obtained for a gas flow ratio O_2/Ar of 3/2 [162]. Several works investigated the microstructure of amorphous V_2O_5 thin films by means of Raman [30,163,164] and FTIR [75] spectroscopy. Lee et al. [163] reported the spectral fingerprint of as-deposited amorphous V_2O_5 films, which exhibit two broad bands at ca. 520 and 650 cm^{-1} assigned to the stretching modes in a disordered V–O–V lattice. The absence of the skeleton mode at 144 cm^{-1} is due to the lack of long-range order. Flash-evaporated V_2O_5 thin films at $25 \leq T_s \leq 200$ °C display a poor crystallization observed by the Raman features, which result in the appearance of the intense external mode at 144 cm^{-1} and ill-resolved internal Raman modes in the high-frequency region [30].

3.5. Electrical properties

V_2O_5 is a n-type semiconductor. Its semiconducting properties are mainly due to the oxygen non-stoichiometry, which are the consequence oxygen vacancies $V_2O_{5-\delta}$. The electrical conductivity of V_2O_5 thin films have been investigated by means of d.c. four-point probe method and a.c. impedance spectroscopy as a function of the deposition parameters and post-annealing treatment [165]. The temperature dependence of the conductivity follows an Arrhenius law in a large range of temperatures. The general condition for semiconducting behavior is that the transition-metal ion could exhibit several valence states such as V^{4+} to V^{5+} in V_2O_5, so that electron hopping takes place between these two levels. If $C = V^{4+}/(V^{4+} + V^{5+})$ is the ratio of the concentration of low valence ions with the total concentration of transition metal ions and A is the average hopping distance, one can estimate the number of charge carriers $N = CA^{-3}$. Using $C \sim 0.02$ and $A = 0.384$ nm, the carrier mobility is quite low lying between 10^{-7} and 10^{-2} $cm^2\ V^{-1}\ s^{-1}$ [166]. Murawski et al. showed that the electrical transport arises from thermally activated hopping that takes place between

the electronic states for V_2O_5 films made by PVD at 840 °C [167] and for amorphous V_2O_5 films obtained by flash evaporation [31]. In V_2O_5, the V^{4+}/V^{5+} ionic pair is bound to positively charged defects, i.e., oxygen vacancies. The removal of an electron from the vacancy and produce a free carrier requests an energy $e^2/\kappa d$. The electrical conductivity is usually described in terms of Mott's theory for electronic transport in transition-metal glasses [168]:

$$\sigma(T) = C(1-C)\frac{\nu_0 e^2}{Ak_BT}\exp(-2\alpha A)\exp\left(\frac{-W}{k_BT}\right) \tag{10}$$

where ν_o is a phonon frequency, and α is the rate of the wave function decay. The thermal activation energy can be expressed as

$$W = W_h + W_d/2 \tag{11}$$

where W_h corresponds to the small polaron formation and W_d to the disorder energy arising from the energy difference of neighboring sites. The separation of W into a polaron and a disorder term is a rather difficult task, which can be partly solved using data taken at low temperatures. Julien et al. [166] reported that oxygen-deficient V_2O_5 films grown at high substrate temperature ($T_s \approx 250$ °C) are highly conductive with $\sigma_e = 10^{-2}$ S cm^{-1} due to the quenching rate ΔT of the films.

Figure 14a,b present the Arrhenius plots of the electrical conductivity σ and the activation energies of flash-evaporated films as a function of the substrate temperature and annealing conditions. These results show that (i) the σ of films deposited at $T_s = 25$ °C is always lower than that of films deposited at higher temperature even after a heat treatment, and (ii) there is a hierarchy in the conductivity such as $\sigma_{ad} < \sigma_{arg} < \sigma_{ox}$, where σ_{ad}, σ_{arg} and σ_{ox} are the conductivities of films as-deposited, annealed in Ar, and annealed in O_2, respectively. The resistivity of an as-grown film at $T_s = 25$ °C is $\rho = 5 \times 10^4$ Ω cm with an activation energy $E_a = 0.43$ eV, whereas that of a film heat-treated in O_2 atmosphere is $\rho = 0.62$ Ω cm with $E_a = 0.15$ eV. We expect that C is a function of T_s and T_a due to the preferable desorption of oxygen during the growth. The increase in σ is attributed to the primary consequence of the structural modification from amorphous to polycrystalline state, and from oxygen deficiency of films grown with smaller O/V ratio at high substrate temperature. Similar effect was observed on the activation energy of the electrical conductivity which decreases with the increase of T_s. Sanchez et al. [167] reported a conductivity of 1.4×10^{-5} S cm^{-1} at 25 °C with an activation energy of $W = 0.41$ eV and a disordered activation energy $W_d = 0.16$ eV for flash-evaporated films. Kumar et al. [82] reported that thermally deposited films at $T_s = 300$ °C exhibit an electrical resistivity of 3.6 Ω cm. Luo et al. [142] studied the impact of the substrate temperature on the electrical properties of sputtered nanostructured films having semiconducting character. Four-point probe measurements show that the square resistance of film decreases exponentially from 46 to 33 kΩ/□ with the increase of T_s from 230 to 320 °C.

Rosaiah et al. [83] reported the effect of T_s on the electrical conductivity of e-beam deposited V_2O_5 films onto ITO-coated flexible Kapton substrate. They showed that σ increases from 2×10^{-6} to 3×10^{-2} S cm^{-1} by the increase of T_s from 30 to 300 °C. Crystalline V_2O_5 thin films (26 nm grain size) deposited by thermal evaporation and annealed at 500 °C exhibited thermoelectric properties with a maximum Seebeck coefficient of −218 μV K^{-1} and electrical conductivity of 0.055 S cm^{-1} [28]. The electrical conductivity was ~10^{-7} S cm^{-1} with a high activation energy E_a = 0.9 eV for sputtered V_2O_5 films (85 nm thick) obtained in O_2/Ar ratio of 20% [169]. Wang et al. [170] demonstrated that a rather thick (200 nm) crystalline V_2O_5 films can work properly as hole-

extraction slab for organic photovoltaic devices. V_2O_5 thin films grown via r.f. reactive sputtering on fused silica substrates showed good electrical response for use as sensors methane and propane (50–3000 ppm) with an activation energy of 0.153 eV and a CPE exponent of n = 1.046, which approximates a CPE due to Debye-like capacitor [171].

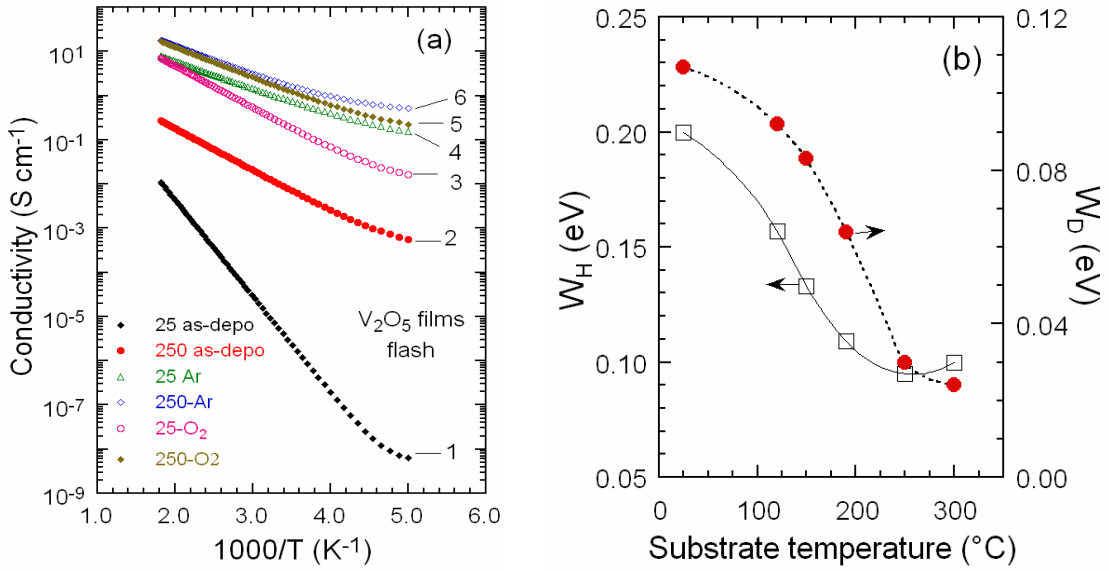

Figure 14. (a) Plots of σT vs. 1/T for flash-evaporated V_2O_5 films obtained in various conditions. (1) as-deposited at T_s = 25 °C, (2) as-deposited at T_s = 250 °C, (3) grown at T_s = 25 °C and annealed in O_2, (4) grown at T_s = 25 °C and annealed in Ar, (5) grown at T_s = 250 °C and annealed in O_2 and (6) grown at T_s = 250 °C and annealed in Ar. The annealing treatment was carried out at 300 °C for 48 h. (b) Plots of σ_{RT} and W_h vs. T_s.

3.6. Intercalation of V_2O_5 films

The Li^+ intercalation into V_2O_5 films has been widely studied on specimens grown on various substrates using all deposition techniques described above. The insertion/de-insertion process occurs in a large potential window 3.5–1.5 V vs. Li^+/Li according the reaction:

$$V_2O_5(\text{orange}) + x\,Li^+ + x\,e^- \leftrightarrow Li_xV_2O_5(\text{green}) \quad (12)$$

where x is the molar fraction of ions and electrons inserted in the host lattice. About $3e^-$ per mole of V_2O_5 could be reached at the end of the discharge (1.5 V), providing a theoretical specific capacity of 442 mAh g^{-1}. The insertion of $3Li^+$ implies the formation of several lithiated phases during discharge with the transitions α→ε ($0 < x < 0.5$), ε→δ ($0 < x < 0.5$), δ→γ ($0 < x < 0.5$) that are characterized by voltage plateaus at 3.4, 3.2 and 2.3 V vs. Li^+/Li, respectively. This is illustrated in Figure 15a for film formed by 50-nm grain size cycled at C/20 rate (20 mA g^{-1} current density). The corresponding cyclic voltammogram is shown in Figure 15b. The irreversible ω-$Li_3V_2O_5$ is formed at the end of the discharge (1.85 V). Subsequent charge appears as a smooth S-shaped voltage profile with a mid-voltage at 2.67 V. As displayed in Figure 15b, four distinctive peaks are observed at 3.30, 3.05, 2.15 and 1.85 V vs. Li^+/Li during a cathodic scan, which is a multi-step Li^+-ion intercalation process. The

corresponding phase transforms from α-V_2O_5 to ε-$Li_{0.5}V_2O_5$ (3.30 V), δ-$Li_1V_2O_5$ (3.05 V), γ-$Li_2V_2O_5$ (2.15 V) and ω-$Li_3V_2O_5$ (1.85 V) represented by the relations:

$$V_2O_5 + 0.5Li + 0.5e^- \rightarrow Li_{0.5}V_2O_5 \quad (13)$$

$$Li_{0.5}V_2O_5 + 0.5Li^+ + 0.5e^- \rightarrow LiV_2O_5 \quad (14)$$

$$LiV_2O_5 + 1Li^+ + 1e^- \rightarrow Li_2V_2O_5 \quad (15)$$

$$Li_2V_2O_5 + 1Li^+ + 1e^- \rightarrow Li_3V_2O_5 \quad (16)$$

In the following anodic scan, one peak is recorded at 2.67 V vs. Li^+/Li corresponding to the delithiation of the ω-$Li_3V_2O_5$ phase.

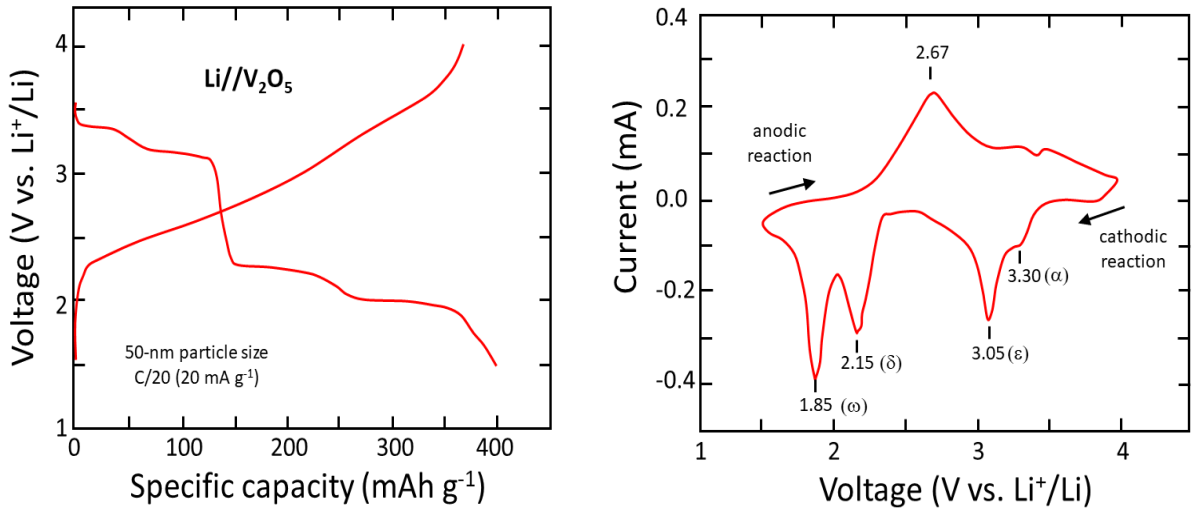

Figure 15. (a) Discharge-charge of Li//V_2O_5 thin-film cell carried out in the potential range 3.6–1.5 V vs. Li^+/Li at C/20 rate (20 mA g^{-1} current density). (b) Cyclic voltammogram showing the formation of the $Li_xV_2O_5$ phases.

The early work of Park et al. [172] showed that spin-coated V_2O_5 xerogel films can accommodate up to 3.3 moles Li/mole V_2O_5 in the potential range 3.8–1.9 V vs. Li^+/Li. The films are highly reversible hosts and deliver a specific energy density 1137 Wh kg^{-1} and specific capacity 1682 C g^{-1}. The Li^+ insertion into V_2O_5 films deposited by CVD, rf-sputtered and ALD techniques onto various substrates such as Pt, Ti, stainless steel, glass and F-doped SnO_2 was studied by Groult et al. [34,35,126,106,108]. Films grown on stainless steel and heat treated at 350 °C show a discharge capacity of 115 mAh g^{-1} at C/23 rate in the potential range 3.8–2.8 V vs. Li^+/Li. The best performances (200 mAh g^{-1} at C/23 rate) were obtained in the electrochemical window 3.8–2.2 V for V_2O_5 deposited onto Ti foil. Jourdani et al. [173] reported an increase of the optical absorption edge from 2.3 to 2.8 eV and the (110) Bragg reflection shift from 2θ = 24.8° to 25.2° for spin coated V_2O_5 intercalated at −0.4 V vs. SCE.

The structural evolution of Li-intercalated V_2O_5 films has been investigated by in situ and ex situ XRD, FTIR and Raman spectroscopy [174–176]. Meulenkamp et al. [177] investigated the different phases of lithiated sol-gel V_2O_5 films in the range $0 \leq x \leq 1.4$ using in situ X-ray diffraction measurements and compared the structural changes with those of V_2O_5 films prepared by other techniques. Spectroscopic studies of Li-intercalated V_2O_5 polycrystalline films have been reported by several groups [71,174,178–180]. Cazzanelli et al. [99] analyzed the Raman spectra of xerogel films intercalated with lithium that showed a significant effect of the water content in the interlayer space inducing new Raman bands at 800 and 950 cm^{-1}. Julien et al. [174] investigated the vibrational modifications of Li intercalated V_2O_5 films deposited by flash evaporation. They proposed that the tensile stress in the $Li_xV_2O_5$ film affects the Raman skeleton mode which shifts from 145 to 154 cm^{-1} due to an increase in the restoring force (Figure 16). Jung et al. [175] confirmed this hypothesis by the correlation of the spectral shift of the Raman mode at 145 cm^{-1} with the stress change as a function of the degree of intercalation in the $Li_xV_2O_5$ lattice.

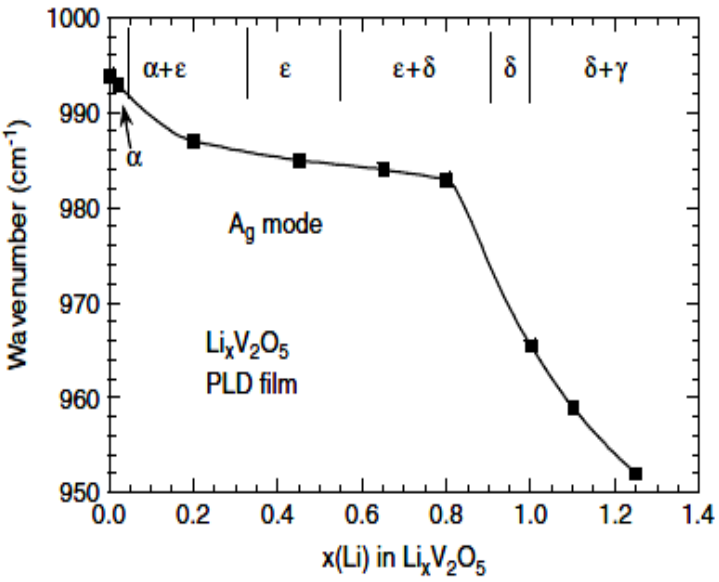

Figure 16. Frequency shift of the A_g vanadyl mode as a function of the lithium insertion in V_2O_5 films grown on Si (1000) wafer. The vibrational spectra reveal that the $Li_xV_2O_5$ phases possess considerably different local symmetry (from Ref. [71]).

Micro-Raman spectroscopy was used to study of electrochemically intercalation $Li_xV_2O_5$ ($0 \leq x \leq 1.8$) samples obtained from V_2O_5 films deposited by various techniques, i.e., ALD and r.f. sputtering. Results showed the phase transformation from α-$Li_xV_2O_5$ to γ-$Li_xV_2O_5$ via ε and δ phases. A linear correlation exists between the $V–O_1$ stretching (vanadyl) mode frequency and the $V–O_1$ bond length in V_2O_5 ALD film [179,180]. Careful examination of the high-frequency region of RS spectra of $Li_xV_2O_5$ shows that, for the Li-rich phase ($0 \leq x \leq 0.5$), the vanadyl stretching mode at 984 cm^{-1} splits into two components, the first one at 975 cm^{-1}, the second at 957 cm^{-1} for $x \geq 0.7$. This is due to the evolution of the local environment of oxygen atoms, i.e., the continuous increase of the interlayer distance with x and it reflects the existence of two different lithium sites [159]. Ramana et al. [71] analyzed the Raman features of the $Li_xV_2O_5$ films prepared by PLD technique in

the range $0.00 \leq x \leq 1.25$. Crystalline V_2O_5 thin films synthesized by means of r.f. sputtering without post-heating treatment were obtained with different crystallographic preferential orientations by changing the growth parameters (T_s and deposition rate) as follows: (i) *h*00-oriented films (*ab* planes perpendicular to the substrate) were prepared at T_s = 300 °C for short time t_d, (ii) longer deposition time at low T_s leads to 110-oriented films and (iii) the 001-oriented films were obtained at high T_s irrespective on t_d [45]. Electrochemical tests of the *h*00-oriented films in Li/EC-DEC–$LiPF_6$/V_2O_5 cells showed specific discharge capacities >300 mAh g^{-1} in the potential range 3.8–1.5 V, with a capacity fading of 3% at C rate over 70 cycles.

Numerous studies of the electrochemical insertion reactions of Li^+ ions in the V_2O_5 film lattice were tested in Li cells with aprotic electrolyte such as 1 mol L-*1* $LiClO_4$ in propylene carbonate (PC) solution or 1 mol L^{-1} $LiPF_6$ in ethylene carbonate (EC):dimethyl carbonate (DMC) (1:1) solution [58,181–186]. Park et al. [187] investigated the discharge capacity of V_2O_5 film cathode as a function of the thickness. Films (230 nm thick) obtained by sputter deposition at power of 100 W in working pressure of 1.3 Pa delivered a specific capacity of ~105 μAh cm^{-2} s^{-1} at current density 500 μA cm^{-2} s^{-1}. Lithium microcells with optimized V_2O_5 films sputtered in O_2/Ar (50/50) atmosphere were investigated by Yoon et al. [58]. When cycled in the range 1.5–3.7 V vs. Li^+/Li, the cell delivered a specific capacity of 125 μAh cm^{-2} μm^{-1} after a first cycle of formation. Nano-porous crystallized V_2O_5 films (~35 nm crystallite size) fabricated by gel electrodeposition with the addition of block copolymer Pluoronic P123 delivered a specific discharge capacity of 240 mAh g^{-1} at 300 mA g^{-1} current density after 40 cycles [188]. Electrochemical studies of V_2O_5 films deposited by spin coating of vanadium-tri(isopropoxide)oxide gel show that the specific capacity and Li^+ diffusion coefficient increased from 4.2×10^{-12} to 6.8×10^{-10} cm^2 s^{-1} in the non-stoichiometric films [189]. Nanostructured V_2O_5 thin films made by anodic deposition from V_2O_5/H_2O_2 solution displayed a large discharge capacity of 596 mAh g^{-1} at a current density of 1.08 A g^{-1} and a fading rate of 1% per cycle in a cell using 1 mol L^{-1} $LiClO_4$ in PC as the electrolyte and a Pt plate as the counter electrode [190]. The V_2O_5 thin film cathode with thickness of ~30 nm fabricated using biological templates delivered specific capacities of ~12 μAh cm^{-2} which is 7–8 times higher than that of planar V_2O_5 cathodes [191]. The effects of ageing on Li intercalation in V_2O_5 films, i.e., the evolution of the SEI, were investigated by a combination of techniques such as cyclic voltammetry, XPS, RBS and AFM for more than 3000 cycles [192].

Kinetics of Li^+ ions in the lattice of V_2O_5 films has been widely studied. Li-ion transport, i.e., ionic conduction (σ_{ion}) and diffusion coefficient (D_{Li}) have been investigated using cyclic voltammetry, galvanostatic titration and electrochemical impedance spectroscopy (EIS) [106,193,194]. D_{Li} varies in the range 6×10^{-10}–2×10^{-11} cm^2 s^{-1} in sol-gel crystalline V_2O_5 thin films (1–3 μm thick) obtained by impedance spectroscopy [195]. Miyazaki et al. [196] investigated D_{Li} of sputtered films oriented along the *a*- and *b*-axis using the chronoamperometry method. Kinetics along the *a*-axis $D_{Li} \approx 10^{-11}$ cm^2 s^{-1} was larger than along the *b*-axis $10^{-13} \leq D_{Li} \leq 10^{-14}$ cm^2 s^{-1}. McGraw et al. [197] obtained D_{Li} vs. *x*(Li) in amorphous V_2O_5 films by PITT measurements on an *h*00 and 110 oriented films made by PLD method. D_{Li} was initially 5×10^{-13} cm^2 s^{-1} and decreased steadily from 1.2×10^{-13} cm^2 s^{-1} at $x = 0.4$ to 5.52×10^{-14} cm^2 s^{-1} at $x = 1.5$ in $Li_xV_2O_5$. Lantelme et al. [106] analyzed the phase transition process controlled by diffusion in V_2O_5 films deposited by CVD method. The component diffusion was estimated as a function of the film thickness: $D_{Li} = 0.48 \times 10^{-12}$ cm^2 s^{-1} for a semi-infinite configuration. D_{Li} was also estimated from both PITT and EIS measurements using a semi-infinite diffusion model [198].

Evolution of the diffusion coefficient D_{Li} in V_2O_5 film (160 nm thick) as a function of the electrode potential is shown in Figure 17. This figure indicates a good agreement between the two techniques.

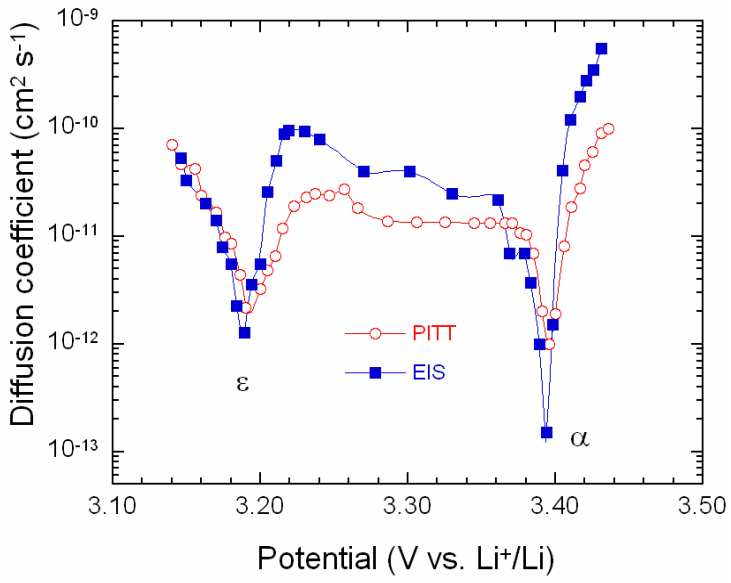

Figure 17. Evolution of the diffusion coefficient of Li^+ ions in the V_2O_5 thin film lattice determined by EIS and PITT assuming a semi-infinite diffusion model (from Ref. [198]).

Pyun and Bae reported a decrease of the diffusion coefficient of xerogel films from 10^{-10} to 10^{-12} cm^2 s^{-1} as the electrode potential fell from 3.0 to 2.2 V vs. Li^+/Li [193]. The transport mechanism was described as a transition from the diffusion-controlled insertion to an interfacial-controlled reaction due to a change of the lattice versus water in $V_2O_5 \cdot nH_2O$ xerogel. Ultrathin (17 nm) V_2O_5 thin were fabricated by spin coating and annealed at at 250 °C for 3 h in a muffle furnace. In the potential range, these films deliver a specific capacity of 262 mAh g^{-1} corresponding to $Li_{1.78}V_2O_5$ when discharge in the potential range from +1 V to −1 V vs. SCE. The capacity loss is 0.03% per cycle over 600 cycles [199]. The effect of porosity on anomalous behavior of the Li intercalation into V_2O_5 film prepared by the polymer (Tergitol from Sigma-Aldrich Co.) surfactant templating method has been studied by AFM and EIS [200]. The diffusion impedance Z_d, which displays a constant phase element (CPE) response can be expressed by:

$$Z_d = \frac{L}{nFAD^{1/2}}\left(\frac{\partial E}{\partial c}\right)(j\omega)^{-\alpha} \tag{17}$$

where L is the film thickness, n the valence of inserted ion, A the active surface, F the Faraday constant, $\partial E/\partial C$ the slope of the coulometric titration and α_d the CPE exponent. Analysis showed that α_d is constant in the frequency range 0.63–0.10 Hz is significantly affected by the surface roughness and the formation of pores with a large size. The chemical diffusion coefficient of 1×10^{-11} cm^2 s^{-1} was suggested. Thin films fabricated by electrostatic spray deposition (ESD) followed by heat treatment at 350 °C in air demonstrated a high energy efficiency. Ultra-high rate capability is obtained at 56C rate with a specific capacity of 86.7 mAh g^{-1} in the potential range 2.5–4.0 V vs. Li^+/Li corresponding to the transitions of three phases: $\alpha \leftrightarrow \varepsilon \leftrightarrow \delta$. When cycled below 2.5 V, these ESD films have poor electrochemical performance due to irreversible structure degradation of the γ-

phase [201,202]. Mui et al. [203] established a relationship between microstructure and kinetics in as-deposited and heat-treated sputtered V_2O_5 thin-film cathodes. D_{Li} was determined by the GITT method for two submicrometric films: finer-grained 80 nm size and coarsed-grained 250 nm size. Both samples display similar values of D_{Li} of 1×10^{-11} for the α-$Li_{0.03}V_2O_5$ phase and 5×10^{-12} cm^2 s^{-1} for the ε-$Li_{0.35}V_2O_5$ and δ-$Li_{0.9}V_2O_5$ phases, whereas D_{Li} in finer-grain film decreases to 1×10^{-13} and 1×10^{-15} cm^2 s^{-1} for the α–ε and ε–δ two-phase systems, respectively. Li^+ diffusion coefficients of electrochemically inserted V_2O_5 films (0.6–3.6 μm thick) deposited by r.f. sputtering with h00 or 110 preferred orientation was studied using EIS measurements [194,204]. The easy diffusivity of Li^+ ions ($2 \times 10^{-11} \leq D_{Li} \leq 3 \times 10^{-10}$ cm^2 s^{-1}) along the b-direction is due to the lattice expansion along the c-axis. The plot D_{Li} vs. x(Li) displays two minima at x = 0.14 and 0.6 that confirm the results of Lu et al. [198]. An energy barrier of 0.98 eV along the *b*-direction was found from the Arrhenius plot of D_{Li} vs.1/T.

4. Doped V_2O_5 films

The poor electrochemical performance of V_2O_5 films during long term cycling attributed to low electronic conductivity can be improved by replacing a dopant for one of the V atoms forming V^{4+} cations [205,206]. Grégoire et al. [207] showed that octahedral chains are formed with metal dopant atoms making stable the structure during electrochemical process. The EXAFS analysis of Cu- and Zn-doped V_2O_5 showed that the environment of vanadium atoms is not altered by the doping atoms (*M*), while new V–O–*M* interactions are triplets [208]. The enhanced stability of M-doped vanadium pentoxide films used as electrode for lithium microbatteries and electrochromic devices comes from the distorted V_2O_5 layered structure. For example, the introduction of Ti dopant in spin-coated V_2O_5 films results in a disturbance of the diffraction peaks of (001) and (002) planes. The formation of V–O–Ti bond opens the interlayer space, distorts the lamellar structure and reduces the oxidation state of V [209]. Numerous metallic ions have been investigated as dopants, including Ag, Fe, Mo, Ta, Mg, Mn, Ti [17,66,93,202,209–214].

Dip-coated Ag-doped V_2O_5 xerogel films with a molar ratio Ag/V in the range 0.005–0.5 showed an increase of the electronic conductivity by 2–3 orders of magnitude that allowed an insertion capacity of 4 Li per mole of $Ag_xV_2O_5$ with an excellent reversibility [215]. $Ag_yV_2O_5$ thin films were prepared by rf magnetron co-sputtering in 14% partial oxygen pressure pO_2 = 14% from metallic Ag and V_2O_5 targets. $Ag_{0.26}V_2O_5$ films were amorphous and showed improved intercalation properties due to the porosity and the additional influence of Ag^+ ions to the redox reaction [205]. Nam et al. [216] investigated the electrochemical properties of copper-doped V_2O_5 thin film prepared by d.c. reactive magnetron co-sputtering within atmosphere O_2:Ar ratio of 10:90. These films were tested as cathode materials in $Cu_xV_2O_5$/Lipon/Li cell and showed stable cycleability beyond 500 cycles with average capacity of 50 μAh cm^{-2} μm^{-1}. Mo-doped V_2O_5 films were grown by thermal evaporation technique onto Ni substrates maintained at T_s = 250 °C and applied as electrode in supercapacitor with 1 mol L^{-1} KCl solution electrolyte. A maximum specific capacity of 175 mF cm^{-2} was obtained for 4 at.% Mo-doped V_2O_5 films [17]. The effect of the annealing temperature on the structure of Mo-doped V_2O_5 films electrochemically deposited resulted in the increase of the interlayer distance from 1.16 nm for as-deposited to 1.38 nm for film annealed at 250 °C that enhanced the Li^+ ion motion in the electrochromic matrix [217].

Tantalum-doped V_2O_5 thin films were deposited by sol-gel dip-coating method using anhydrous isopropyl alcohol as solvent [211]. 5 mol% Ta doped films as counter-electrode for electrochromic device exhibited a charge density of 70 mC cm^{-2} with high stability up to 1500 cycles. Mg-doped V_2O_5 films deposited by RF magnetron reactive sputtering onto SnO_2-coated glass substrates were studied for various amount of dopant. Low Mg content (2 at.%) enhanced the specific discharge capacity and the diffusion coefficient of Li^+ inserted ions, while high Mg content (15 at.%) favored the electrochromic window and the switching response time [212].

Molybdenum acts as a n-type dopant in V_2O_5 that results in an increase of the carrier concentration and a shift of the absorption edge towards shorter wavelengths [93]. Several techniques were used to prepare V_2O_5 doped with Mn such as electrodeposition [218], e-beam evaporation [219], and dip-coating [213].

Mn-doped V_2O_5 films were fabricated by dip-coating route with post-annealing at 250 ℃ in air for 3 h using ~1.67% of $Mn(Ac)_2{\cdot}4H_2O$ as Mn^{2+} source. Structural and elemental analyses showed that: (i) Mn doping suppresses the orthorhombic symmetry, (ii) V^{4+} and V^{5+} coexist, (iii) the formation of oxygen vacancies is due to the increase in the Mn^{2+} cation size. The suggested formula was $(Mn,V)_2O_{4.74}(V_{\ddot{O}})_{0.26}$. The intercalation/deintercalation process is enhanced by the oxygen vacancies that eliminate the phase transition and reduce the irreversible capacity [182,213].

Sn-doped V_2O_5 films were obtained by drop-casting and further heat treatment at 450 ℃ in air for 2 h. As measured by XPS experiments, the 10% Sn^{4+} ions accommodation is compensated by the reduction of V^{+5} to V^{4+} ions. The introduction of Sn atoms causes a slight expansion of the unit volume due to the small lattice expansion along *a*- and *c*-direction, which indicates the presence of Sn^{4+} ions between the VO_5 layers, forming SnO_6 octahedra [220]. Ce-doped V_2O_5 films prepared by sol-gel route and annealed at 400 ℃ showed a phase transition from α-V_2O_5 orthorhombic to β-V_2O_5 tetragonal structure. Film doped with 1 mol.% Ce exhibited the best ion storage capacity of ~207 mC cm^{-2} [221]. Titanium doped V_2O_5 films have been widely investigated as intercalation hosts for electrochromic devices [209,214,222–225]. Sol-gel dip-coated $(100 - x)V_2O_5{\cdot}xTiO_2$ films as electrochromic electrodes were formed with Ti content up to 20 mol.% by reacting vanadium and titanium tetra-isopropoxide as precursors [214]. The best results were obtained for the proper amount of Ti dopant (5 mol.%) showing that 550 nm-thick films switched with a coloration from pale yellow to a greenish state when reduced with 5.4 mC cm^{-2} of lithium. Wei et al. [209] reported a remarkable improved stability of the WO_3-based electrochromic devices using Ti-doped V_2O_5 films. The device utilizing the optimized V_2O_5:Ti electrode (V:Ti = 2:1) lasted 200,000 cycles in the transmittance range 2–62% without degradation. An increase of the Li intercalation capacity from 14 to 27 mC cm^{-2} for 5% Ti-doped V_2O_5 films prepared by spin coating of inorganic sol-gel precursors was attributed to the non-stoichiometry and the smaller grain size [222]. Lee and Cao [223] demonstrated an Li^+ intercalation performance improved by 100% in 20 mol.% Ti-doped V_2O_5 polycrystalline films that results from interaction force between adjacent V_2O_5 slabs. Highly stable V_2O_5–TiO_2 films fabricated by sol-gel electrodeposition [224,225] were proposed as electrochromic windows using PProDOT-Me_2 that is poly (3,3-dimethyl-3,4-dihydro-2H thieno[3,4b][1,4]-di-oxepine). Tungsten-doped V_2O_5 films were deposited by rf magnetron sputtering on non-alkali glass substrate. Due to their good thermal insulation function, these films were applied as self-cleaning windows or anti-fogging glasses. The optimal thermal insulation temperature is 19.3 ℃ for 3 wt.% W-doped V_2O_5 thin films [226].

5. Nanocomposite films

V_2O_5-based nanocomposite films have been fabricated for several applications, such as electrochromic devices and gas sensors. Such a nanocomposite was obtained with V_2O_5 obtained from an aqueous solutions of equimolar vanadium chloride and ammonium tungstate and F-doped SnO_2-coated glass substrates maintained at T_s = 400 °C. Coloration efficiency (CE) of ~49 cm^2 C^{-1} was obtained for a film mixed with 15% WO_3 which is stable up to 1000 cycles [227]. Thin (240 nm) and thick (485 nm) V_2O_5–MoO_3 films were deposited on conducting (SnO_2:F) glass by e-beam (3 kV) and thermal vacuum deposition (EBD and TVD, respectively) for opto-electronic applications [228]. A specific capacity of 80 μAh cm^{-2} s^{-1} after 70 cycles in the potential range 1.5–3.9 V vs. Li^+/Li was delivered by MoO_3–V_2O_5 nanocomposite thin film electrodes deposited by r.f. sputtering from dual targets [229]. Mixed V_2O_5–WO_3 thin films were deposited by pulsed spray pyrolysis technique onto glass [227]. Sol-gel deposited $(1 - x)WO_3 \cdot xV_2O_5$ films at x = 0.035 showed the best electrochromic performance with a brownish blue [230]. Thin films of $(V_2O_5)_{1-x} \cdot (MoO_3)_x$ ($0 \leq x \leq 1$) were fabricated by e-beam evaporation in $p(O_2) = 2 \times 10^{-2}$ mPa and T_s = 150 °C. The optical bandgap increases and the electrical conductivity decreased with the increase of composition x [231]. V_2O_5–28 at.% MoO_3 TVD thick films deposited onto borosilicate glass were amorphous, while thin films were crystalline (crystallite size 38 nm) with strong reflections along (131), (160) and (270) direction. The bandgap varies linearly with the atomic wt.% of MoO_3 in V_2O_5–MoO_3 EBD thin films, i.e., from 2.35 eV for 10 wt.% to 2.70 eV for 90 wt.%. Composite V_2O_5 xerogel films assembled with polypyrrole (PPy) showed high electrical conductivity and fast electrochemical response that makes them candidates for redox sensor in flow injection analysis [232]. Graphene/V_2O_5/MoO_3 nanocomposite film was synthesized by dip-coating via sol-gel preparation of the precursors. This composite shows fast switching electrochromic performances with bleaching time of 1.25 s and the coloration time of 1.40 s [20]. V_2O_5/graphene nanocomposite films prepared by direct intercalation method using V_2O_5 sol and graphene were developed for their use in fast switching electrochromic devices. The intercalation of graphene improves the stability and the optical reversibility of the films, i.e., 1.5 times larger than that of V_2O_5 xerogel, due to the fast electron mobility of 1.5×10^4 cm^2 V^{-1} s^{-1} in graphene [233]. Thin film electrodes for supercapacitors were made of V_2O_5/carbon nanotubes composites. A symmetric capacitor formed by identical V_2O_5/CNT electrodes operates in a wide potential range of 1.6 V in aqueous electrolyte delivering a volumetric energy density of 41 Wh dm^{-3} [234]. V_2O_5 xerogel films were modified by poly(ethylene-oxide) (PEO). The inserted structure is modified the interaction of hydrogens with oxygens of the V–O bonds that shields the interaction between Li^+ ions and V_2O_5 slabs resulting in an improved anodic electrochromic property [235].

6. Applications

The early potential applications of nanostructured V_2O_5 were found in the field of lithium-ion batteries [236,237], thin-film microbatteries [12,108,238], actuators [239], catalysis [240], humidity sensors [241], electrochromic display devices [139,242], optical switching memories [243], antirelection coating [81].

6.1. Li microbatteries

Since the work of Bates et al. [12], V_2O_5 thin films have been extensively investigated as positive electrodes (so-called cathodes) in rechargeable lithium microbatteries constituted by a lithium metal anode, an amorphous inorganic electrolyte and amorphous or crystalline V_2O_5 [244]. The most popular solid-electrolyte thin film $Li_{2.9}PO_{3.3}N_{0.46}$ (named Lipon) was deposited by r.f. magnetron sputtering of Li_3PO_4 in N_2 ambient. Its ionic conductivity is 2×10^{-6} S cm^{-1} at 25 °C [245,246]. A typical solid-state battery (SSB) is built by 1 µm thick amorphous V_2O_5 film deposited at 25 °C, a 1 µm thick solid electrolyte and 5 µm thick lithium film (5 times in excess) [247,248]. Currently, thin-film cells are evaluated at different current densities and their delivered capacity is expressed by surface and thickness in mC cm^{-2} µm^{-1} or µAh cm^{-2} µm^{-1}. Considering the theoretical specific capacity of 440 mAh g^{-1} for $Li_xV_2O_5$ with uptake of 3 Li per formula and the density d = 3.36 g cm^{-3} of V_2O_5, the theoretical specific capacity is Q_{th} = 147.8 µAh cm^{-2} µm^{-1} for a film as dense as the crystalline material. The schematic cross-section of a thin-film lithium microbattery is presented in Figure 18.

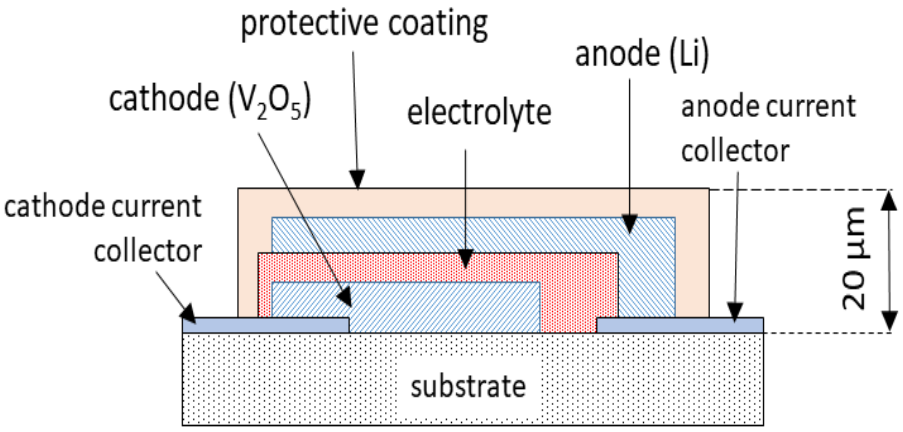

Figure 18. Schematic cross-section of a thin-film lithium microbattery.

Prior Li//V_2O_5 cell cycled in the potential window 3.6–1.5 V delivered a capacity ~100 µAh cm^{-2} µm^{-1} at 10 µA cm^{-2} [12]. Vanadium oxide films (VO_x) prepared by several techniques such as PECVD, PLD, rf-sputtering at the National Renewable Energy Lab. (USA) exhibit high discharge capacity and are highly stable during electrochemical cycling. Both crystalline and amorphous PLD V_2O_5 films (T_s = 200 °C) deliver a discharge specific capacity of 380 mAh g^{-1}, while for the most stable films prepared by PECVD and exhibiting an O/V ratio close to that of V_6O_{13} (0.5 µm thick) the discharge capacity exceeds 408 mAh g^{-1} over 4400 cycles. These results indicate that the PECVD technology is very attractive for manufacturing rechargeable lithium microbatteries [62,67]. Typical experimental conditions for the deposition of a thin-film battery made by r.f. sputtering are summarized in Table 2 [249,250]. A solid-state film cell including a crystalline V_2O_5 cathode (2.4 µm thick), a Lipon electrolyte film (1.4 µm thick) and a lithium metal film (3.5 µm thick) operated in the potential 3.8–2.15 V vs. Li^+/Li. Figure 19 displays the discharge-charge profiles of the SSB at 10 µA cm^{-2} current density. After the first cycle of formation (SEI

formation), a stable specific capacity of 30 μAh cm^{-2} was obtained with a cathode film 2.4 μm thick [250].

Table 2. Experimental conditions for the deposition of thin-film battery active materials [250].

Component	Target	Power density (W cm^{-2})	Gas (sccm)	Deposition pressure (Pa)
V_2O_5	Vanadium	4.5	Ar:O_2 (50:5)	0.55
Lipon	Li_3PO_4	2.2	N_2 (80)	2
Lithium	Li	Thermal evaporation		

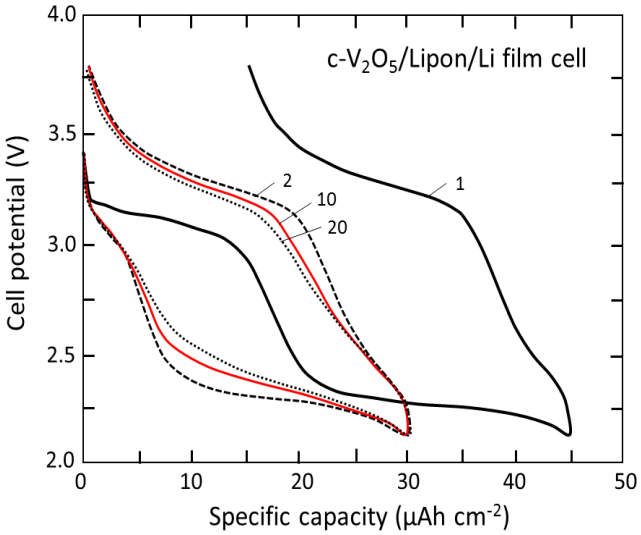

Figure 19. Discharge-charge profiles of a c-V_2O_5/Lipon/Li SSB cycled between 3.8 and 2.15 V at 10 μA cm^{-2} current density (from Ref. [250]).

Optimized conditions for rf-sputtering deposition (T_s = 250 °C, P_w = 50 W) provide discharge capacity of 30.2 μAh cm^{-2} μm^{-1} with two potential plateaus at 3.5–3.6 V that corresponds to the Li uptake $0 < x < 1$ in $Li_xV_2O_5$. Assuming a gravimetric density of 2.5 g cm^{-3} for rf-sputtered films, the discharge capacity is 121 mAh g^{-1}. A capacity loss of 0.0076% per cycle was reported over 2000 cycles [251]. V_2O_5 thin films obtained by electrostatic spray-deposition (ESD) onto Pt substrates from triisopropoxy-vanadium oxide in 0.05 mol L^{-1} ethyl alcohol solution were tested in Li cells with 1 mol L^{-1} $LiClO_4$/propylene carbonate (PC) as electrolyte. The crystallized films annealed at 275 °C exhibit a good cycleability and high capacity of 270 mAh g^{-1} at a current rate of 0.2C. After 25 cyles at 1C rate the capacity remains stable at 260 mAh g^{-1} [252]. Navone et al. [253] reported the fabrication of all-solid-state lithium microbatteries using crystalline sputtered V_2O_5 thin film (1.2 μm thick) as cathode and lithium phosphorus oxynitride (Lipon) (1 μm thick) as solid electrolyte. The electrochemical performances are strongly affected by the cathode morphology; its porosity depends on the oxygen flow during the film deposition; thus, a 0.6 μm thick porous film was optimized using an oxygen flow of 12.5 sccm ($p(O_2)$ = 0.05 Pa). Such a microcell film showed a stable discharge capacity of 35 μAh cm^{-2} at a current density of 10 μA cm^{-2} between 3.8 and 2.15 V vs. Li^+/Li. Electrochemical performance of 50 μAh cm^{-2} was obtained with the use of a 1 μm thick dense film. All-solid-state thin-film lithium cells with the configuration Li/Lipon/$Li_xV_2O_5$/Cu were fabricated on

stainless steel (SS) substrate using sequential deposition techniques. The amorphous V_2O_5 cathode film was lithiated by vacuum evaporation of pure Li metal to form the $Li_{1.3}V_2O_5$ cathode film (500 nm thick). The microbattery was formed during the first charging cycle, where lithium anode was electroplated in between the Lipon electrolyte layer and the stainless-steel substrate. These "Li-free" cells (1 cm^2 active area) delivered a specific capacity of 43 mAh cm^{-2} μm^{-1} at a current density of 0.1 mA cm^{-2} in the potential range 3.8–1.8 V vs. Li^+/Li and showed a good stable cycleability up to 770 cycles at 0.1 mA cm^{-2} current density [254]. All-solid-state microbatteries $Li_{1.5}V_2O_5$/Lipon/Li were fabricated by the successive deposition of active elements on Si/Ti substrate as follows: (i) the substrate was first coated with 0.2 m thick gold film to form a current collector; (ii) crystalline $Li_xV_2O_5$ films with x = 0.8 and 1.5 (1 μm thick) were prepared by thermal evaporation of metallic lithium (0.2 μm thick) deposited on a magnetron sputtered pristine material. This cathode element was keep at rest for 5 days to ensure the diffusion of Li ions into the V_2O_5 matrix; (iii) the in situ solid electrolyte film was obtained by reactive sputtering of Li_3PO_4 in N_2 atmosphere ($p(N_2)$ = 2 Pa) at a power of 350 W to ensure a deposition rate of 034 μm h^{-1}; (iv) the Li anode (3.5 μm thick) was obtained by thermal evaporation at growth rate of 150 nm min^{-1}. The all-solid-state microbattery delivered a typical specific capacity of 50 μAh cm^{-2} in the potential range 2.15–3.80 V vs. Li^+/Li [255].

V_2O_5 thin films prepared by means of cathodic deposition from V_2O_5 and H_2O_2 in aqueous show excellent electrochemical properties as cathodes. The films had a specific discharge capacity of 240 mA h g^{-1} retained after 200 cycles with a 1.3C rate (200 mA g^{-1}) that corresponds to an energy density of 723 Wh kg^{-1}. Even at high 70C rate, V_2O_5 film electrodes retained a good discharge capacity of 120 mAh g^{-1} [104]. Ostreng et al. [113] reported remarkable electrochemical properties of strongly structured ALD V_2O_5 films as cathodes in Li microbatteries. The best performance was obtained a discharge rate of 120C for more than 1500 cycles for 10-nm nanostructured film. McGraw et al. [197] investigated the intercalation mechanism in $Li_xV_2O_5$ thin films deposited by by pulsed laser deposition and estimated the chemical diffusion coefficients $\tilde{D}$ of Li^+ ions from potentiostatic intermittent titration technique (PITT) measurements. $\tilde{D}$ varies in the range from 1.7×10^{-12} cm^2 s^{-1} to 5.8×10^{-15} cm^2 s^{-1} in crystalline PLD films, while $\tilde{D} = 5 \times 10^{-13}$ cm^2 s^{-1} in amorphous V_2O_5 films. The general trend is a decrease of $\tilde{D}$ upon Li intercalation in the host lattice reaching the final value of 5.5×10^{-14} cm^2 s^{-1} at $Li_{1.5}V_2O_5$ (δ phase). The specific discharge capacity 334 mAh g^{-1} of 10% Sn-doped V_2O_5 film is twice that of pure V_2O_5 film [220]. This superior electrochemical performance is attributed the stabilization of VO_5 slabs by Sn^{4+} ions that produces higher diffusion coefficient of Li^+ ions. High-rate V_2O_5-based Li-ion thin film polymer cells show outstanding long-term cyclability. Cathode thin film growth was performed by r.f. sputtering (power 100 W) in high vacuum (1 mPa) at the 1.3 Pa partial pressure of the Ar/O_2 gas mixture (ratio 2:1) [256]. The V_2O_5/solid polymer/Li cells were electrochemically tested in the potential range 2.5–3.8 V at current regimes ranging from 1.5C to 10C. Stable specific capacity of 100 mAh g^{-1} was maintained up to 5C after 300 cycles.

Recent developments of V_2O_5 thin films as cathode elements of rechargeable microbatteries shows the general trends of amorphous films. Zeng et al. [257] reported that films prepared via sol-gel and liquid deposition method show a gradual activation upon cycling that yields higher capacity (~200 mAh g^{-1} after 200 cycles) and faster kinetics. This good performance was attributed to the novel nanostructure obtained from mild synthesis conditions. Mattelaer et al. [258,259] prepared amorphous films by ALD technique based on tetrakis[ethylmethylamino]vanadium in combination

with water and ozone. Galvanostatic charging and discharging performed at 1C in the potential range 3.5–2.9 V (LiV_2O_5) and 4.0–1.5 V ($Li_3V_2O_5$), the thin films cells deliver volumetric capacities of 488 and 810 mAh cm^{-3}, respectively. Chae et al. [260] compared the electrochemical features of amorphous (a-V_2O_5) and crystalline (c-V_2O_5) films. The high performance of a-V_2O_5 with a reversible specific capacity >600 mAh g^{-1} at 13C rate was attributed to the absence of irreversible phase transitions and lithium ions trapping. This remarkable rate property for a-V_2O_5 films is due to the vacant sites that open the Li^+ diffusion pathways [261]. Zhang et al. [238] made a all-solid-state battery V_2O_5/Lipon/$LiCoO_2$ prepared by r.f. magnetron sputtering in which the V_2O_5 (200 nm thick) acts as anode film. This microbattery (1.03 μm thick) delivered a volumetric capacity of 9.5 μAh cm^{-2} μm^{-1} after 40 cycles.

6.2. Supercapacitors

Electrochemical capacitors (ECs) known as "supercapacitors" employ the electrical double-layer phenomenon to store energy. There are two subclasses of ECs: the electrochemical double-layer capacitors (EDLCs) having a non-faradaic charge character and the pseudocapacitors based on faradaic electrochemical redox reaction. Among transition-metal oxides used as ECs electrode, V_2O_5 has attracted attention because of its pseudocapacitive features, broad oxidation states and high specific capacitance 294 F g^{-1}. Reports on the properties of V_2O_5 thin films as electrodes for supercapacitors are rather sparse [17,234,262,263]. Films deposited onto Ni substrates by dc-magnetron sputtering in O_2:Ar (1:8) atmosphere and grown with predominant (001) orientation are composed of 32-nm grain size and surface roughness of 14 nm. These films exhibit high specific capacitance of 238 F g^{-1} at current density of 1 mA cm^{-2} [263]. 4 at.% MoO_3-doped V_2O_5 films obtained by thermal evaporation on Ni substrates, in which Mo atoms substitute for V, exhibit a specific capacitance of 175 F g^{-1} [17]. Wu et al. [234] fabricated V_2O_5/CNT films in three steps: (i) mixture of carbon nanotubes (CNTs) and V_2O_5 with ethyl cellulose in ethanol and terpilenol as uniform and viscous slurry, (ii) evaporation of ethanol and "doctor blade" coating onto alumina substrate and (iii) annealing at 350 ℃. Reversible redox reaction was evidenced by cyclic voltammetry providing a specific capacitance of 216 F g^{-1} at 5 mV s^{-1} that is 5.2 times of that of CNTs (41 F g^{-1}) and a volumetric capacitance of ≈460 F cm^{-3}. This electrode maintains a power density of 22.2 kW L^{-1}.

6.3. Electrochromic devices

A typical electrochromic device (ECD) includes an electrochromic layer, an electrolyte layer and an ion storage layer. Both electrochromic and storage layers are deposited on transparent substrates coated by transparent conductive film. ECDs operate by a change in optical properties between different colors. V_2O_5 is utilized as a counter electrode material in ECDs [22,65,96,264–269]. During the optical switching, it provides electrochemical redox reactions that balance charge transfer at the electrochromic working electrode. The typical electrochromic reaction of V_2O_5 can be expressed by the double injection of ions and electrons (Eq 12). The transmittance variance (ΔT) is defined by [270]:

$$\Delta T(\%) = T_b - T_c \tag{18}$$

where T_b and T_c are the transmittances (in %) of bleached and colored states, respectively. The coloration efficiency (*CE*) is defined as the change in the optical density (ΔOD) per unit of electrode area (A) at a given wavelength, as follows:

$$CE = \Delta OD/(q/A) = \log(T_b/T_c)/(q/A) \tag{19}$$

where q is the inserted charge capacity and the color efficiency (η) is defined by:

$$\eta = \Delta OD/q \tag{20}$$

Following the work of Sarminio et al. [271] there is a close correlation between the stress change in the crystalline film and the electrochromic properties. Tensile stress varies with the x(Li) composition, the largest obtains with the δ-LiV_2O_5 phase. V_2O_5 thin film electrochemically deposited onto ITO glass from a poly-vanadic acid sol were used in ECD cell [272]. The cell was tested more than 8×10^4 times and its response time was 2–20 s, depending upon the cell voltage. Shimizu et al. [273] developed an electrochromic display device using V_2O_5 thin film deposited by spin coating of V_2O_5 powder dissolved into a mixed solution of benzyl alcohol and iso-butanol. The films coated onto ITO glass followed by annealing at $T_a > 300$ °C are crystalline and exhibit excellent reversibility of the electrochromism. Mesoporous V_2O_5 films prepared by hydrolysis of vanadium tri-isopropoxide in the presence of polyethylene glycol (PEG) have shown that the surfactant promotes the formation of micrometric crystallites highly suitable for the development of advanced ECDs [274]. V_2O_5 thin films deposited by means of microwave plasma MOCVD have a transmittance of 70% at 400 nm absorption edge. The reversible Li intercalation reaction occurs with a change in the film color from yellow (V_2O_5) to blue (LiV_2O_5) [37]. The addition of the organic–inorganic template 3-isocyanatopropyltriethoxysilane (ICS) and poly(propylene glycol) bis-2(ammino-propyl-ether) (2-APPG) in sol-gel deposited V_2O_5 electrochromic thin film implements the storage capacity and increases the diffusivity of Li^+ ions by modification of the surface structure of the film [275]. Magnetron sputtered V_2O_{5-z} thin films onto flexible polyethylene terephthalate/indium tin oxide (PET/ITO) substrates at oxygen flow rate of 2 sccm were oxygen deficient with $z = 0.169$ and offered a light modulation of 43.3%. After 200 cycles, at wavelength of 400 nm, an optical density change and color efficiency of 0.38 and 102.5 $cm^2\ C^{-1}$ were obtained, respectively [276]. Similar ECD devices were fabricated at 23 °C by Lin and Tsai [19], showing an oxygen deficiency $z = 0.13$ and a transmittance modulation of 36.5% at wavelength of 400 nm.

Recent studies show that high switching speed and coloration efficiency are obtained for titanium-doped V_2O_5 thin film electrochromic devices [277] and spray-deposited lithium-doped V_2O_5 [278]. The ammonium intercalated V_2O_5 xerogel thin film prepared at 50 and 85 °C show two-step color changes: yellow/green and green/blue related to the redox process of V^{4+}/V^{5+} states [96].

6.4. Gas sensors

Because of their excellent catalytic properties, V_2O_5 thin films have attracted great interest as gas sensors. The adsorbtion of gaseous molecules and catalytic reactions are due to the active sites formed by V^{5+} ions with d^0 electronic configuration [279,280]. Especially in thin film form, V_2O_5 is used in sensor of volatile organic compounds (VOCs) emitted by industries such as benzene, toluene, acetone, methanol, xylene, etc. that are hazardous substances to human health [70,281–287]. For a short review of V_2O_5-based resistive gas sensors, see Ref. [171]. Nanocrystalline V_2O_5 thin films

deposited by a spray pyrolysis technique at T_s = 300 ℃ had a preferential orientation along the (001) direction and revealed the highest sensing response in the presence of ethanol vapor [280]. Nanocrystalline V_2O_5 thin films synthesized by the ethanol suspension were developed as solid-state sensors. A reversible reaction occurs with ammonia with the formation of ammonium metavanadate (bleaching), which is turn back to the starting state after annealing in air at 350 ℃ [279]. The polycrystalline V_2O_5 films prepared by spray pyrolysis were found to be highly sensitive towards VOCs. The selective nature of the films deposited at T_s = 300 ℃ are shown in Figure 20 [92].

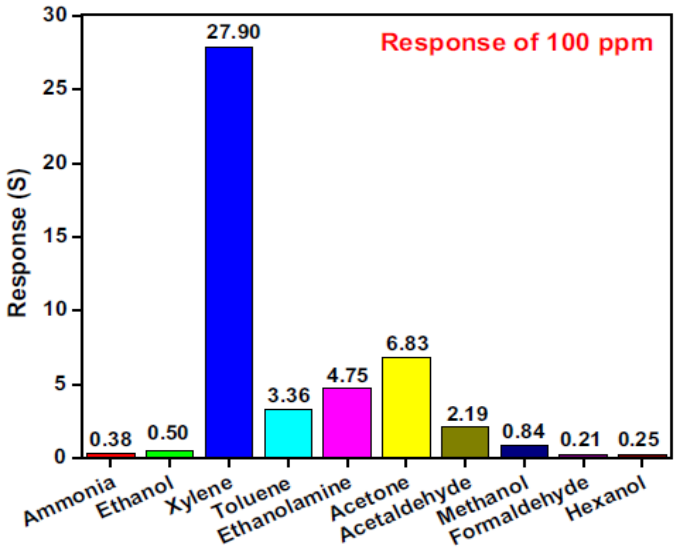

Figure 20. Response of V_2O_5 films prepared bybspray pyrolysis at T_s = 300 ℃ for different VOCs vapors at concentration of 100 ppm (from [92]).

V_2O_5 films fabricated by PLD technique were characterized as ammonia sensors even in the presence of NO used in diesel engine exhaust [70]. V_2O_5 thin films 200–600 nm thick were fabricated at 290 ℃ on fused silica and alumina by means of rf reactive sputtering from a metallic vanadium target for use as gas sensor. Thin films exhibit good response towards hydrogen (5–300 ppm), methane and propane (50–3000 ppm) [171]. Ultrathin crystalline epitaxial V_2O_5 films (10–90 nm thick) were deposited onto c-Al_2O_3 by ALD method with oxygen plasma. The films exhibiting a (001) preferred orientation are used as humidity sensors [119]. Nanostructured V_2O_5 films deposited by dc reactive magnetron sputtering have also been proposed as 2-propanol vapor sensors with an excellent response towards 5–200 ppm under ambient atmosphere [287].

6.5. Healthy and safety issues

A very detailed review (210 pages) on the toxicity of V_2O_5 can be found on the web site [287]. In short, V_2O_5 is toxic, and it is specified on the U.S. National Library of Medecine [288] that probable oral lethal dose for humans is between 5 and 50 mg/kg or between 7 drops and 1 teaspoonful for a 70 kg (150 lb.) person. In practice, however, there is little occasion to eat such an amount of vanadium pentoxide and absorption can occur in humans following inhalation exposure. In this case, V_2O_5 is readily absorbed through the lungs. The effects from exposure may include

burns to the skin and eyes, tracheitis, bronchitis, emphysema, pulmonary edema, or bronchial pneumonia. The American Conference of Governmental Industrial Hygienists (ACGIH) has established a threshold limit value time-weighted average (TLV TWA) of 0.05 mg/cu m for respirable dust. When absorbed, V_2O_5 is eliminated, mainly by urine. In practice, the protection against this product thus concerns people who have to manipulate or prepare it in factories since they are placed in situation where over-exposure may occur. The hygiene and safety policy of laboratories and institutions that are concerned is given in [288].

While hygiene and safety policy practice when handling or dealing with V_2O_5, this material plays an increasing role to make progress in environmental pollution and industrial safety issue, owing to its use for gas sensing application, reviewed in [289]. The list of targeted gas is constantly increasing [286].

7. Concluding remarks

V_2O_5 is one of the most important material for many applications, including optical switching devices, gas and humidity sensors, smart widows, window for solar cell, photocatalysis, for electrochromic devices [82], color filters [146], reflectance mirrors, gas sensors, surfaces with tunable emittance for temperature control of space vehicles [81,147], thermochromic thin films for optoelectronic applications [93]. Nanocrystal V_2O_5 thin film used as hole-extraction layer in normal architecture organic solar cells demonstrated the potential of this material for photovoltaic applications [170], and W-doped V_2O_5 film can be used for thermal insulation [226].

So many applications explain the huge amount of works devoted to the preparation of V_2O_5 thin films. The difficulty is that their properties are strongly dependent of the mode of preparation, the film thickness, the orientation of the film, the crystallinity, the purity, the substrate [84], the nature and amount of dopants, the packing density of the film [85], temperature of the substrate [142], deposition rate, in short, deposition conditions [96], post-annealing treatment [217], the choice of precursors [100], porosity [188,201,262], doping.

As electrochromic device, Ti-doped V_2O_5 electrode has lasted 200,000 cyclic switching times between the lowest (2%) and highest (62%) transmittance with no significant degradation of performance [209]. Nevertheless, V_2O_5 alone cannot be commercialized as an electrochromic device, because of its low electrical conductivity, poor coloration efficiency and narrow color variation. However, these drawbacks can be overcome by combining V_2O_5 with other compounds. A recent example is the graphene/V_2O_5/MoO_3 film, which combines the richer colors of MoO_3, the high conductivity of graphene and the remarkable electrochromic properties of V_2O_5. Such films present multi-electrochromic behavior (yellow → green → blue → gray-brown), excellent electrochromic performance, with tranmittence variation of 25.35%, bleaching time of 1.25 seconds, coloration time 1.40 seconds. In addition, it demonstrates good cycling [20]. Such films are thus very good fast switching electrochromic materials. Recently, the growth of large-scale electrodes by atmospheric pressure chemical vapor deposition has been made possible, with good performance for electrochromic devices with a change in optical density per unit inserted charge density reaches 336 $cm^2\ C^{-1}$ at 630 nm, with a diffusion coefficient for the lithium as large as $9.19 \times 10^{-11}\ cm^2\ s^{-1}$ [33].

For use as a supercapacitors, nano-structured V_2O_5 is needed to increase the surface area. In particular, a grain size of 148 nm of the deposited film exhibited a high rate pseudo capacitance of

730 mF cm^{-2} at 1 mA cm^{-2} of current density [27]. Note the result was also obtained under such synthesis conditions that led to a c-axis oriented structure, giving better results than a (201) orientation. A film electrode composed of intertwined V_2O_5 nanowires and carbon nanotubes (CNTs) demonstrated a volumetric capacitance of ≈460 F cm^{-3} [234]. A capacity of 397 F g^{-1} was obtained after ultrasonic weltering [262]. V_2O_5 thin films with 4 at.% of Mo doping exhibited a maximum specific capacitance of 175 mF/cm^2 at current density of 1 mA/cm^2 [17].

Regarding the electrochemical properties, high energy density (900 W h kg^{-1} at 200 mA g^{-1}), power density (28 kW kg^{-1} at 10.5 A g^{-1}), good cyclic stability over 200 cycles have been obtained with nanostructured V_2O_5 thin-film electrodes prepared by cathodic deposition [104,190]. These results, as well as results obtained by atomic layer deposition [111,113,114] show so that V_2O_5 nano-electrodes can now be used with high power and energy densities for thin film Li-ion batteries.

V_2O_5 is also increasingly used as sensor. Fit has been tested for longer time periods up to 100 h as ammonia sensors. Very stable behavior was found with detection limit of 80 ppb for NH_3 both in dry and humid air. The detection limits for NO and CO were 20 ppm and 50 ppm, respectively. The results suggest that the vanadium oxide thin-film sensing layers are good candidates for a Selective Catalytic Reduction (SCR) process control application [70]. The room temperature gas sensing response of V_2O_5 films was found to be highly selective towards xylene [92]. They also exhibited good response towards hydrogen (5–300 ppm), methane and propane (50–3000 ppm) [171]. Recently, intrinsic thermochromism of V_2O_5 films was reported as a perceptible thermally induced color change from bright yellow to deep orange [290].

All these recent results show the continuous improvement in the synthesis of the films and the performance for tehes applications. In most of the works that have been published, however, the optimization of the film is made within one deposition technique, for one application. Therefore, further works should address two questions. The first one is to determine which deposition technique and synthesis parameters are best suited for each application. For instance, electrochemical properties of vanadium oxide are reported to be optimized for highly crystallized V_2O_5 [21], but better kinetics and higher volumetric capacities were observed for the amorphous vanadium oxides compared to their crystalline counterparts in Ref. [259]. Therefore, further works are needed to clarify the conditions that optimize the films for electrochemical applications. The second question is which kind of film should be used to optimize the film as a function of the application that is targeted. For instance, low Mg-doping (2%) is preferred for lithium ion battery applications, but 15% Mg-doping is preferred for electrochromic applications [212]. Only very few such reports have been made to relate the synthesis to applications, and further works along these lines would be very useful in the near future.

Conflict of interest

The authors declare that there is no conflict of interest regarding the publication of this manuscript.

References

1. Roscoe HE (1868) XXXVI.—Researches on vanadium. *J Chem Soc* 21: 322–350.

2. Ditte A (1885) Recherches sur le vanadium, propriétés de l'acide vanadique. *C R Acad Sci Paris* 101: 698–702.
3. Hugues JM, Finger LW (1983) The crystal chemistry of shcherbinaite, naturally occurring V_2O_5. *Am Mineral* 68: 1220–1222.
4. Ketelaar JAA (1936) Crystal structure and shape of colloidal particles of vanadium pentoxide. *Nature* 137: 316.
5. Byström A, Wilhelmi KA, Brotzen O (1950) Vanadium pentoxide—a compound with five-coordinated vanadium atoms. *Acta Chem Scand* 4: 1119–1130.
6. Bachmann HG, Ahmed FR, Barnes WH (1961) The crystal structure of vanadium pentoxide. *Z Krist-Cryst Mater* 115: 110–131.
7. Enjalbert R, Galy J (1986) A refinement of the structure of V_2O_5. *Acta Crystallogr* C 42: 1467–1469.
8. Ramana CV, Hussain OM, Srinivasulu-Naidu B, et al. (1997) Spectroscopic characterization of electron-beam evaporated V_2O_5 thin films. *Thin Solid Films* 305: 219–226.
9. Julien C, Guesdon JP, Gorenstein A, et al. (1995) The influence of the substrate material on the growth of V_2O_5 flash-evaporated films. *Appl Surf Sci* 90: 389–391.
10. Balog P, Orosel D, Cancarevic Z, et al. (2007) V_2O_5 phase diagram revisited at high pressures and high temperatures. *J Alloy Compd* 429: 87–98.
11. Parija A, Prendergast D, Banerjee S (2017) Evaluation of multivalent cation insertion in single- and double-layered polymorphs of V_2O_5. *ACS Appl Mater Inter* 9: 23756–23765.
12. Bates JB, Dudney NJ, Lubben DC, et al. (1995) Thin-film rechargeable lithium batteries. *J Power Sources* 54: 58–62.
13. Julien C, Gorenstein A (1995) Materials design and optimization for thin-film microbatteries. *Ionics* 1: 193–210.
14. Julien C (1996) Technology of microbatteries and its applications, In: Radhakrishna S, *Trends in Materials Science*, New Delhi: Narosa Publ. House, 24–43.
15. Julien C (2000) Lithium microbatteries, In: Julien C, Stoynov Z, *Materials for lithium-ion batteries*, Amsterdam: Kluwer Acad Publ., 381–400.
16. Lampert CM (1998) Smart switchable glazing for solar energy and daylight control. *Sol Energ Mat Sol C* 52: 207–221.
17. Prakash NG, Dhananjaya M, Reddy BP, et al. (2016) Molybdenum doped V_2O_5 thin films electrodes for supercapacitors. *Mater Today Proc* 3: 4076–4081.
18. Vernardou D, Sapountzis A, Spanakis E, et al. (2013) Electrochemical activity of electrodeposited V_2O_5 coatings. *J Electrochem Soc* 160: D6–D9.
19. Lin YS, Tsai CW (2008) Reactive sputtering deposition of V_2O_{5-z} on flexible PET/ITO substrates for electrochromic devices. *Surf Coat Tech* 202: 5641–5645.
20. Ma X, Lu S, Wan F, et al. (2016) Synthesis and electrochromic characterization of graphene/V_2O_5/MoO_3 nanocomposite films. *ECS J Solid State Sc* 5: P572–P577.
21. Vernardou D, Loudoudakis D, Spanakis E, et al. (2014) Electrochemical properties of vanadium oxide coatings grown by hydrothermal synthesis on FTO substrates. *New J Chem* 38: 1959–1964.
22. Mjejri I, Manceriu LM, Gaudon M, et al. (2016) Nano-vanadium pentoxide films for electrochromic displays. *Solid State Ionics* 292: 8–14.

23. Beke S (2011) A review of the growth of V_2O_5 films from 1885 to 2010. *Thin Solid Films* 519: 1761–1771.
24. Rao MC, Rao RK (2014) Thermal evaporated V_2O_5 thin films: thermodynamic properties. *Int J Chem Tech Res* 6: 3931–3934.
25. Chakraborty S, Sakata H, Yokoyama E, et al. (2007) Laser induced forward transfer technique for maskless patterning of amorphous V_2O_5 thin films. *Appl Surf Sci* 254: 638–643.
26. Kumar RTR, Karunagaran B, Venkatachalam S, et al. (2003) Influence of deposition temperature on the growth of vacuum evaporated V_2O_5 thin films. *Mater Lett* 57: 3820–3825.
27. Dhananjaya M, Prakash NG, Sandhya GL, et al. (2017) Microstructure and supercapacitor properties of V_2O_5 thin film prepared by thermal evaporation method. *Mech Mater Sci Eng*.
28. Santos R, Loureiro J, Nogueira A, et al. (2013) Thermoelectric properties of V_2O_5 thin films deposited by thermal evaporation. *Appl Surf Sci* 282: 590–594.
29. Julien C, Khelfa A, Benramdane N, et al. (1994) Lithium insertion in indium selenide films: application to microbatteries. *Mater Sci Eng B-Adv* 23: 105–115.
30. Julien C, Guesdon JP, Gorenstein A, et al. (1995) The growth of V_2O_5 flash-evaporated films. *J Mater Sci Lett* 14: 934–936.
31. Murawski L, Gledel C, Sanchez C, et al. (1987) Electrical conductivity of V_2O_5 and $Li_xV_2O_5$ amorphous thin films. *J Non-Cryst Solids* 89: 98–106.
32. Ramana CV, Hussain OM, Naidu BS, et al. (1998) Physical investigations on electron-beam evaporated vanadium pentoxide films. *Mater Sci Eng B-Adv* 52: 32–39.
33. Vernardou D (2017) Using an atmospheric pressure chemical vapor deposition process for the development of V_2O_5 as an electrochromic material. *Coatings* 7: 24.
34. Mantoux A, Groult H, Balnois E, et al. (2004) Vanadium oxide films synthesized by CVD and used as positive electrodes in secondary lithium batteries. *J Electrochem Soc* 151: A368–A373.
35. Groult H, Le Van K, Mantoux A, et al. (2007) Study of the Li^+ insertion into V_2O_5 films deposited by CVD onto various substrates. *J Power Sources* 174: 312–320.
36. Barreca D, Armelao L, Caccavale F, et al. (2000) Highly oriented V_2O_5 nanocrystalline thin films by plasma-enhanced chemical vapor deposition. *Chem Mater* 12: 98–103.
37. Watanabe H, Itoh K, Matsumoto O (2001) Properties of V_2O_5 thin films deposited by means of plasma MOCVD. *Thin Solid Films* 386: 281–285.
38. Barreca D, Battiston GA, Caccavalec F, et al. (1999) A PE-MOCVD route to V_2O_5 nanostructured thin films. *J Phys IV France* 9: 529–536.
39. Crociani L, Carta G, Natali M, et al. (2011) MOCVD of vanadium oxide films with a novel vanadium(III) precursor. *Chem Vapor Depos* 17: 6–8.
40. Sahana MB, Shivashankar SA (2004) Metalorganic chemical vapor deposition of highly oriented thin film composites of V_2O_5 and V_6O_{13}: suppression of the metal-semiconductor transition in V_6O_{13}. *J Mater Res* 19: 2859–2870.
41. Robbins J, Seman M (2005) Electrochromic devices deposited on low-temperature plastics by plasma-enhanced chemical vapor deposition. United States: USDOE Office of Energy Efficiency and Renewable Energy (EERE), Report No.: FG36-04GO14328.
42. Nandakumar NK, Seebauer EG (2011) Low temperature chemical vapor deposition of nanocrystalline V_2O_5 thin films. *Thin Solid Films* 519: 3663–3668.
43. Koike S, Fujieda T, Sakai T, et al. (1999) Characterization of sputtered vanadium oxide films for lithium batteries. *J Power Sources* 81–82: 581–584.

44. Batista C, Teixeira V, Carneiro J (2008) Structural and morphological characterization of magnetron sputtered nanocrystalline vanadium oxide films for thermochromic smart surfaces. *J Nano Res* 2: 21–30.
45. Quinzeni I, Ferrari S, Quartarone E, et al. (2011) Structural, morphological and electrochemical properties of nanocrystalline V_2O_5 thin films deposited by means of radiofrequency magnetron sputtering. *J Power Sources* 196: 10228–10233.
46. Giannetta HMR, Calaza C, Lamas DG, et al. (2015) Electrical transport properties of V_2O_5 thin films obtained by thermal annealing of layers grown by RF magnetron sputtering at room temperature. *Thin Solid Films* 589: 730–734.
47. Poelman H, Tomaszewski H, Poelman D, et al. (2002) V_2O_5 thin films deposited by means of dc magnetron sputtering from ceramic V_2O_3 targets. *Surf Interface Anal* 34: 724–727.
48. Su Q, Lan W, Wang YY, et al. (2009) Structural characterization of β-V_2O_5 films prepared by dc reactive magnetron sputtering. *Appl Surf Sci* 255: 4177–4179.
49. Fateh N, Fontalvo GA, Mitterer C (2007) Structural and mechanical properties of dc and pulsed dc reactive magnetron sputtered V_2O_5 films. *J Phys D Appl Phys* 40: 7716–7719.
50. Gallasch T, Stockhoff T, Baither D, et al. (2011) Ion beam sputter deposition of V_2O_5 thin films. *J Power Sources* 196: 428–435.
51. Silversmit G, Poelman H, DeGryse R (2004) Influence of magnetron deposition parameters on the stoichiometry of sputtered V_2O_5 films. *Surf Interface Anal* 36: 1163–1166.
52. De Castro MSB, Ferreira CL, de Avillez RR (2013) Vanadium oxide thin films produced by magnetron sputtering from a V_2O_5 target at room temperature. *Infrared Phys Techn* 60: 103–107.
53. Raj PD, Gupta S, Sridharan M (2015) Nanostructured V_2O_5 thin films deposited at low sputtering power. *Mat Sci Semicon Proc* 39: 426–432.
54. Fateh N, Fontalvo GA, Cha L, et al. (2008) Synthesis-structure relations for reactive magnetron sputtered V_2O_5 films. *Surf Coat Tech* 202: 1551–1555.
55. Lourenço A, Gorenstein A, Passerini S, et al. (1998) Radio-frequency reactively sputtered VO_x thin films deposited at different oxygen flows. *J Electrochem Soc* 145: 706–711.
56. Benmoussa M, Ibnouelghazi E, Bennouna A, et al. (1995) Structural, electrical and optical properties of sputtered vanadium pentoxide thin films. *Thin Solid Films* 265: 22–28.
57. Benmoussa M, Outzourhit A, Bennouna A, et al. (2002) Electrochromism in sputtered V_2O_5 thin films: structural and optical studies. *Thin Solid Films* 405: 11–16.
58. Yoon YS, Kim JS, Choi SH (2004) Structural and electrochemical properties of vanadium oxide thin films grown by d.c. and r.f. reactive sputtering at room temperature. *Thin Solid Films* 460: 41–47.
59. Ottaviano L, Pennisi A, Simone F, et al. (2004) RF sputtered electrochromic V_2O_5 films. *Opt Mater* 27: 307–313.
60. Lin YS, Tsai CW, Chen PW (2008) Electrochromic properties of V_2O_{5-z} thin films sputtered onto flexible PE/ITO substrates. *Solid State Ionics* 179: 290–297.
61. Kang M, Chu M, Kim SW, et al. (2013) Optical and electrical properties of V_2O_5 nanorod films grown using an electron beam. *Thin Solid Films* 547: 198–201.
62. Zhang JG, McGraw JM, Turner J, et al. (1997) Charging capacity and cycling stability of VO_x films prepared by pulsed laser deposition. *J Electrochem Soc* 144: 1630–1634.

63. Julien C, Haro-Poniatowski E, Camacho-Lopez MA, et al. (1999) Growth of V_2O_5 thin films by pulsed laser deposition and their applications in lithium microbatteries. *Mater Sci Eng B-Adv* 65: 170–176.
64. Ramana CV, Smith RJ, Hussain OM, et al. (2004) On the growth mechanism of pulsed-laser deposited vanadium oxide thin films. *Mater Sci Eng B-Adv* 111: 218–225.
65. Iida Y, Kaneko Y, Kanno Y (2008) Fabrication of pulsed-laser deposited V_2O_5 thin films for electrochromic devices. *J Mater Process Tech* 197: 261–267.
66. Iida Y, Kanno Y (2009) Doping effect of M (M = Nb, Ce, Nd, Dy, Sm, Ag, and/or Na) on the growth of pulsed-laser deposited V_2O_5 thin films. *J Mater Process Tech* 209: 2421–2427.
67. McGraw JM, Perkins JD, Hasoon F, et al. (2000) Pulsed laser deposition of oriented V_2O_5 thin films. *J Mater Res* 15: 2249–2265.
68. Ashrafi MA, Ranjbar M, Kalhori H, et al. (2017) Pulsed laser deposition of Mo–V–O thin films for chromogenic applications. *Thin Solid Films* 621: 220–228.
69. Madhuri KV, Rao KS, Naidu BS, et al. (2002) Characterization of laser ablated V_2O_5 thin films. *J Mater Sci-Mater El* 13: 426–432.
70. Huotari J, Bjorklund R, Lappalainen J, et al. (2015) Pulsed laser deposited nanostructured vanadium oxide thin films characterized as ammonia sensors. *Sensor Actuat B-Chem* 217: 22–29.
71. Ramana CV, Smith RJ, Hussain OM, et al. (2005) Surface analysis of pulsed laser-deposited V_2O_5 thin films and their lithium intercalated products studied by Raman spectroscopy. *Surf Interface Anal* 37: 406–411.
72. Ramana CV, Smith RJ, Hussain OM (2003) Grain size effects on the optical characteristics of pulsed-laser deposited vanadium oxide thin films. *Phys Status Solidi A* 199: R4–R6.
73. Beke S, Giorgio S, Korosi L, et al. (2008) Structural and optical properties of pulsed laser deposited V_2O_5 thin films. *Thin Solid Films* 516: 4659–4664.
74. Fang GJ, Liu ZL, Wang YQ, et al. (2000) Orientated growth of V_2O_5 electrochromic thin films on transparent conductive glass by pulsed excimer laser ablation technique. *J Phys D Appl Phys* 33: 3018–3021.
75. Ramana CV, Hussain OM, Pinto R, et al. (2003) Microstructural features of pulsed-laser deposited V_2O_5 thin films. *Appl Surf Sci* 207: 135–138.
76. Ramana CV, Smith RJ, Hussain OM, et al. (2004) Growth and surface characterization of V_2O_5 thin films made by pulsed laser deposition. *J Vac Sci Technol A* 22: 2453–2458.
77. Ramana CV, Hussain OM, Naidu BS, et al. (1997) Influence of substrate temperature on the composition and structural properties of electron beam evaporated V_2O_5 thin films. *Vacuum* 48: 431–434.
78. Ramana CV, Hussain OM (1997) Optical absorption behaviour of vanadium pentoxide thin films. *Adv Funct Mater* 7: 225–231.
79. Ramana CV, Hussain OM, Naidu BS, et al. (1998) Physical investigations on electron-beam evaporated vanadium pentoxide films. *Mater Sci Eng B-Adv* 52: 32–39.
80. Ramana CV, Hussain OM, Naidu BS (1997) Growth and structure of electron beam evaporated V_2O_5 thin films. *Mater Chem Phys* 50: 195–199.
81. Ramana CV, Hussain OM, Uthanna S, et al. (1998) Influence of oxygen partial pressure on the optical properties of electron beam evaporated vanadium pentoxide thin films. *Opt Mater* 10: 101–107.

82. Kumar A, Singh P, Kulkarni N, et al. (2008) Structural and optical studies of nanocrystalline V_2O_5 thin films. *Thin Solid Films* 516: 912–918.
83. Rosaiah P, Sandhya GL, Suresh S, et al. (2016) Effect of substrate temperature on micro-structural, optical and electrical properties of V_2O_5 thin films. *Adv Mater Proc* 1: 215–219.
84. Thiagarajan S, Thaiyan M, Ganesan R (2015) Physical property exploration of highly oriented V_2O_5 thin films prepared by electron beam evaporation. *New J Chem* 39: 9471–9479.
85. Ali HM, Abdel-Kakeem AM (2010) Structural and optical properties of electron-beam evaporated Al_2O_3-doped V_2O_5 thin films for various applications. *Phys Status Solidi A* 207: 132–138.
86. Bouzidi A, Benramdane N, Nakrela A, et al. (2002) First synthesis of vanadium oxide thin films by spray pyrolysis technique. *Mater Sci Eng B-Adv* 95: 141–147.
87. Boudaoud L, Benramdane N, Desfeux R, et al. (2006) Structural and optical properties of MoO_3 and V_2O_5 thin films prepared by spray pyrolysis. *Catal Today* 113: 230–234.
88. Varadaraajana V, Satishkumara BC, Nandab J, et al. (2011) Direct synthesis of nanostructured V_2O_5 films using solution plasma spray approach for lithium battery applications. *J Power Sources* 196: 10704–10711.
89. Irani R, Rozati SM, Beke S (2013) Structural and optical properties of nanostructural V_2O_5 thin films deposited by spray pyrolysis technique: effect of the substrate temperature. *Mater Chem Phys* 139: 489–493.
90. Wei Y, Li M, Zheng J, et al. (2013) Structural characterization and electrical and optical properties of V_2O_5 films prepared via ultrasonic spraying. *Thin Solid Films* 534: 446–451.
91. Abd-Alghafour NM, Ahmed NM, Hassan Z, et al. (2016) Influence of solution deposition rate on properties of V_2O_5 thin films deposited by spray pyrolysis technique. *AIP Conf Proc* 1756: 090010.
92. Vijayakumar Y, Kumar-Mani G, Ramana-Reddy MV, et al. (2015) Nanostructured flower like V_2O_5 thin films and its room temperature sensing characteristics. *Ceram Int* 41: 2221–2227.
93. Nazemiyan M, Jalili S (2013) Record low temperature Mo doped V_2O_5 thermochromic thin films for optoelectronic applications. *AIP Adv* 3: 112103.
94. Akl AA (2006) Effect of solution molarity on the characteristics of vanadium pentoxide thin films. *Appl Surf Sci* 252: 8745–8750.
95. Wang J, Curtis CJ, Schulz DL, et al. (2004) Influences of treatment temperature and water content on capacity and rechargeability of V_2O_5 xerogel films. *J Electrochem Soc* 151: A1–A7.
96. Najdoski M, Koleva V, Samet A (2014) Effect of deposition conditions on the electrochromic properties of nanostructured thin films of ammonium intercalated vanadium pentoxide xerogel. *J Phys Chem C* 118: 9636–9646.
97. Chen Y, Xie K, Liu Z (1998) XPS studies of V_2O_5 thin film at different temperatures and oxygen partial pressures. *Appl Surf Sci* 126: 347–351.
98. Wang Y, Shang H, Chou T, et al. (2005) Effects of thermal annealing on the Li^+ intercalation properties of $V_2O_5 \cdot nH_2O$ xerogel films. *J Phys Chem B* 109: 11361–11366.
99. Cazzanelli E, Mariotto G, Passerini S, et al. (1996) Raman spectroscopic investigations of Li-intercalated V_2O_5 xerogel. *J Non-Cryst Solids* 208: 89–98.
100. Gokdemir FP, Ozdemir O, Kutlu K (2014) Comparison of structural and electrochemical properties of V_2O_5 thin films prepared by organic/inorganic precursors. *Electrochim Acta* 121: 240–244.

101. Raj DV, Ponpandian N, Mangalaraj M, et al. (2013) Effect of annealing and electrochemical properties of sol-gel dip coated nanocrystalline V_2O_5 thin films. *Mat Sci Semicon Proc* 16: 256–262.
102. Wang Y, Cao G (2006) Li^+-intercalation electrochemical/electrochromic properties of vanadium pentoxide films by sol electrophoretic deposition. *Electrochim Acta* 51: 4865–4872.
103. Kim KH, Roh DK, Song IK, et al. (2010) Enhanced performance as a lithium ion battery cathode of electrodeposited V_2O_5 thin films by e-beam irradiation. *J Solid State Electr* 14: 1801–1805.
104. Liu Y, Clark M, Zhang Q, et al. (2011) V_2O_5 nano-electrodes with high power and energy densities for thin film Li-ion batteries. *Adv Energy Mater* 1: 194–202.
105. Groult H, Balnois E, Mantoux A, et al. (2006) Two-dimensional recrystallisation processes of nanometric vanadium oxide thin films grown by atomic layer chemical vapor deposition (ALCVD) evidenced by AFM. *Appl Surf Sci* 252: 5917–5925.
106. Lantelme F, Mantoux A, Groult H, et al. (2002) Analysis of a phase transition process controlled by diffusion, application to lithium insertion into V_2O_5. *Electrochim Acta* 47: 3927–3938.
107. Keränen J, Auroux A, Ek S, et al. (2002) Preparation, characterization and activity testing of vanadia catalysts deposited onto silica and alumina supports by atomic layer deposition. *Appl Catal A-Gen* 228: 213–225.
108. Le Van K, Groult H, Mantoux A, et al. (2006) Amorphous vanadium oxide films synthesized by ALCVD for lithium rechargeable batteries. *J Power Sources* 160: 592–601.
109. Musschoot J, Deduytsche D, Poelman H, et al. (2009) Comparison of thermal and plasma-enhanced ALD/CVD of vanadium pentoxide. *J Electrochem Soc* 156: P122–P126.
110. Badot J, Ribes S, Yousfi E, et al. (2000) Atomic layer epitaxy of vanadium oxide thin films and electrochemical behavior in presence of lithium ions. *Electrochem Solid St* 3: 485–488.
111. Chen X, Pomerantseva E, Banerjee P, et al. (2012) Ozone-based atomic layer deposition of crystalline V_2O_5 films for high performance electrochemical energy storage. *Chem Mater* 24: 1255–1261.
112. Badot JC, Mantoux A, Baffier N, et al. (2004) Electrical properties of V_2O_5 thin films obtained by atomic layer deposition (ALD). *J Mater Chem* 14: 3411–3415.
113. Ostreng E, Gandrud KB, Hu Y, et al. (2014) High power nano-structured V_2O_5 thin film cathodes by atomic layer deposition. *J Mater Chem A* 2: 15044–15051.
114. Chen X, Pomerantseva E, Gregorczyk K, et al. (2013) Cathodic ALD V_2O_5 thin films for high-rate electrochemical energy storage. *RSC Adv* 3: 4294–4302.
115. Blanquart T, Niinisto J, Gavagnin M, et al. (2013) Atomic layer deposition and characterization of vanadium oxide thin films. *RSC Adv* 3: 1179–1185.
116. Daubert JS, Lewis NP, Gotsch HN, et al. (2015) Effect of meso- and micro-porosity in carbon electrodes on atomic layer deposition of pseudocapacitive V_2O_5 for high performance supercapacitors. *Chem Mater* 27: 6524–6534.
117. Santos L, Swiatowska J, Lair V, et al. (2017) Mechanisms of enhanced lithium intercalation into thin film V_2O_5 in ionic liquids investigated by X-ray photoelectron spectroscopy and time-of-flight secondary ion mass spectroscopy. *J Power Sources* 364: 61–71.
118. Wang X, Guo Z, Gao Y, et al. (2017) Atomic layer deposition of vanadium oxide thin films from tetrakis(dimethylamino)vanadium precursor. *J Mater Res* 32: 37–44.

119. Sreedhara MB, Ghatak J, Bharath B, et al. (2017) Atomic layer deposition of ultrathin crystalline epitaxial films of V_2O_5. *ACS Appl Mater Inter* 9: 3178–3185.
120. Chain EE (1991) Optical properties of vanadium dioxide and vanadium pentoxide thin films. *Appl Optics* 30: 2782–2787.
121. Cezar AB, Graff IL, Varalda J, et al. (2014) Oxygen-vacancy-induced room-temperature magnetization in lamellar V_2O_5 thin films. *J Appl Phys* 116: 163904.
122. Ranea VA, Dammig-Quina PL (2016) The structure of the bulk and the (001) surface of V_2O_5. A DFT + U study. *Mater Res Express* 3: 085005.
123. Chakrabarti A, Hermann K, Druzinic R, et al. (1999) Geometric and electronic structure of vanadium pentoxide: a density functional bulk and surface study. *Phys Rev B* 59: 10583–10590.
124. Eyert V, Hck KH (1998) Electronic structure of V_2O_5: role of octahedral deformations. *Phys Rev B* 57: 12727–12737.
125. Audière JP, Madi A, Grenet JC (1982) Electrical and thermal properties of highly quenched amorphous V_2O_5 thin films. *J Mater Sci* 17: 2973–2978.
126. Kumagai N, Kitamoto H, Baba M, et al. (1998) Intercalation of lithium in rf-sputtered vanadium oxide film as an electrode material for lithium-ion batteries. *J Appl Electrochem* 28: 41–48.
127. Benmoussa M, Outzourhit A, Jourdani R, et al. (2003) Structural, optical and electrochromic properties of sol-gel V_2O_5 thin films. *Active Passive Electron Comp* 26: 245–256.
128. Losurdo M, Barreca D, Bruno G, et al. (2001) Spectroscopic ellipsometry investigation of V_2O_5 nanocrystalline thin films. *Thin Solid Films* 384: 58–64.
129. Vernardou D, Paterakis P, Drosos H, et al. (2011) A study of the electrochemical performance of vanadium oxide thin films grown by atmospheric pressure chemical vapour deposition. *Sol Energ Mat Sol C* 95: 2842–2847.
130. Guimond S, Sturm JM, Göbke D, et al. (2008) Well-ordered V_2O_5(001) thin films on Au(111): growth and thermal stability. *J Phys Chem C* 112: 11835–11846.
131. Szörényi T, Bali K, Hevesi I (1980) Structural characterization of amorphous vanadium pentoxide thin films prepared by chemical vapour deposition. *J Non-Cryst Solids* 35–36: 1245–1248.
132. Özer N (1997) Electrochemical properties of sol-gel deposited vanadium pentoxide films. *Thin Solid Films* 305: 80–87.
133. Kumar RTR, Karunagaran B, Kumar VS, et al. (2003) Structural properties of V_2O_5 thin films prepared by vacuum evaporation. *Mat Sci Semicon Proc* 6: 543–546.
134. Gilles E, Boesman E (1966) EPR studies of V_2O_5 single crystals. I. Defect centres in pure, non-stoichiometric vanadium pentoxide. *Phys Stat Solidi B* 14: 337–347.
135. Pozarnsky G, Wright L, McCormijk A (1994) Effects of aging time on V_2O_5 sol-gel coatings. *J Sol-Gel Sci Techn* 3: 57–62.
136. Senapati S, Panda S (2016) Effect of aging of V_2O_5 sol on properties of nanoscale films. *Thin Solid Films* 599: 42–48.
137. Anaissi FJ, Demets GJF, Alvarez EB, et al. (2001) Long-term aging of vanadium(V) oxide xerogel precursor solutions: structural and electrochemical implications. *Electrochim Acta* 47: 441–450.
138. Hirashima H, Gengyo M, Kojima C, et al. (1995) Effects of aging and drying on structure of V_2O_5 gels. *J Non-Cryst Solids* 186: 54–58.

139. Talledo A, Granqvist CG (1995) Electrochromic vanadium-pentoxide-based films: structural, electrochemical and optical properties. *J Appl Phys* 77: 4655–4666.
140. Luksich J, Aita CH (1991) Annealing response of disordered sputter deposited vanadium pentoxide (V_2O_5). *J Vac Sci Technol* A 9: 542–546.
141. Song GY, Oh C, Sinha S, et al. (2017) Facile phase control of multivalent vanadium oxide tin films (V_2O_5 and VO_2) by atomic layer deposition and postdeposition annealing. *ACS Appl Mater Inter* 9: 23909–23917.
142. Luo Z, Wu Z, Xu X, et al. (2010) Impact of substrate temperature on the microstructure, electrical and optical properties of sputtered nanoparticle V_2O_5 thin films. *Vacuum* 85: 145–150.
143. El Sound AMA, Mansour B, Soliman LI (1994) Optical and electrical properties of V_2O_5 thin films. *Thin Solid Films* 247: 140–143.
144. Akl AA (2010) Thermal annealing effect on the crystallization and optical dispersion of sprayed V_2O_5 thin films. *J Phys Chem Solids* 71: 223–229.
145. Maki K, Fukuda T, Momose H, et al. (2012) Structural and optical properties of reactive-sputtered films of V_2O_5: measurement of optical bandgap and roughness correction. *J Fac Sci Tech Seikei Univ* 49: 41–44.
146. Atuchin VV, Ayupov BM, Kochubey VA, et al. (2008) Optical properties of textured V_2O_5/Si thin films deposited by reactive magnetron sputtering. *Opt Mater* 30: 1145–1148.
147. Wu QH, Thissen A, Jaegermann W, et al. (2004) Photoelectron spectroscopy study of oxygen vacancy on vanadium oxides surface. *Appl Surf Sci* 236: 473–478.
148. Wu QH, Thißen A, Jaegerman W (2005) Photoelectron spectroscopic study of Li intercalation into V_2O_5 thin films. *Surf Sci* 578: 203–212.
149. Benayad A, Martinez H, Gies A, et al. (2006) Vanadium pentoxide thin films used as positive electrode in lithium microbatteries: an XPS study during cycling. *J Phys Chem Solids* 67: 1320–1324.
150. Swiatowska-Mrowiecka J, Martin F, Maurice V, et al. (2008) The distribution of lithium intercalated in V_2O_5 thin films studied by XPS and ToF-SIMS. *Electrochim Acta* 53: 4257–4266.
151. Salvi AM, Guascito MR, DeBonis A, et al. (2003) Lithium intercalation on amorphous V_2O_5 thin film, obtained by r.f. deposition, using in situ sample transfer for XPS analysis. *Surf Interface Anal* 35: 897–905.
152. Ibris N, Salvi AM, Liberatore M, et al. (2005) XPS study of the Li intercalation process in sol-gel-produced V_2O_5 thin film: influence of substrate and film synthesis modification. *Surf Interface Anal* 37: 1092–1104.
153. Alamarguy D, Castle JE, Ibris N, et al. (2006) Characterization of sol-gel crystalline V_2O_5 thin films after Li intercalation cycling. *Surf Interface Anal* 38: 801–804.
154. Fleutot B, Martinez H, Pecquenard B, et al. (2008) Surface film morphology (AFM) and chemical features (XPS) of cycled V_2O_5 thin films in lithium microbatteries. *J Power Sources* 180: 836–844.
155. Alamarguy D, Castle JE, Liberatore M, et al. (2006) Distribution of intercalated lithium in V_2O_5 thin films determined by SIMS depth profiling. *Surf Interface Anal* 38: 847–850.
156. Julien CM, Massot M (2003) Lattice vibrations of materials for lithium rechargeable batteries III. Lithium manganese oxides. *Mater Sci Eng B-Adv* 100: 69–78.

157. Julien CM, Massot M (2003) Lattice vibrations of materials for lithium rechargeable batteries I. Lithium manganese oxides. *Mater Sci Eng B-Adv* 97: 217–230.
158. Abello L, Husson E, Repelin Y, et al. (1983) Vibrational spectra and valence force field of crystalline V_2O_5. *Spectrochim Acta A* 39: 641–651.
159. Baddour-Hadjean R, Pereira-Ramos JP, Navone C, et al. (2008) Raman microspectrometry study of electrochemical lithium intercalation into sputtered crystalline V_2O_5 thin films. *Chem Mater* 20: 1916–1923.
160. Surca A, Orel B, Drazic G, et al. (1999) Ex situ and in situ infrared spectroelectrochemical investigations of V_2O_5 crystalline films. *J Electrochem Soc* 146: 232–242.
161. Fang GJ, Liu ZL, Wang Y, et al. (2001) Synthesis and structural, electrochromic characterization of pulsed laser deposited vanadium oxide thin films. *J Vac Sci Technol A* 19: 887–892.
162. Su Q, Liu Q, Ma ML, et al. (2008) Raman spectroscopic characterization of the microstructure of V_2O_5 films. *J Solid State Electr* 12: 919–923.
163. Lee SH, Cheong HM, Seong MJ, et al. (2002) Microstructure study of amorphous vanadium oxide thin films using Raman spectroscopy. *J Appl Phys* 92: 1893–1897.
164. Lee SH, Cheong HM, Seong MJ, et al. (2003) Raman spectroscopic studies of amorphous vanadium oxide thin films. *Solid State Ionics* 165: 111–116.
165. Zhang Y, Liu YW, Cheng YS, et al. (2005) Electrochemical impedance spectra of V_2O_5 xerogel films with intercalation of lithium ion. *J Cent South Univ T* 12: 309–314.
166. Julien C, Khelfa A, Guesdon JP, et al. (1996) Electrical properties of flash-evaporated V_2O_5 films. *Ionics* 2: 380–385.
167. Sanchez C, Livage J, Audiere JP, et al. (1984) Influence of the quenching rate on the properties of amorphous V_2O_5 thin films. *J Non-Cryst Solids* 65: 285–300.
168. Mott NF (1968) Conduction in glasses containing transition metal ions. *J Non-Crystal Solids* 1: 1–17.
169. Akl AA (2007) Crystallization and electrical properties of V_2O_5 thin films prepared by RF sputtering. *Appl Surf Sci* 253: 7094–7099.
170. Wang HQ, Li N, Guldal NS, et al. (2012) Nanocrystal V_2O_5 thin film as hole-extraction layer in normal architecture organic solar cells. *Org Electron* 13: 3014–3021.
171. Schneider K, Lubecka M, Czapla A (2016) V_2O_5 thin film for gas sensor applications. *Sensor Actuat B-Chem* 236: 970–977.
172. Park HK, Smyrl WH, Ward MD (1995) V_2O_5 xerogel films as intercalation hosts for lithium. *J Electrochem Soc* 142: 1068–1073.
173. Jourdani R, Jadoual L, Ait El Fqih M, et al. (2018) Effects of lithium insertion and deinsertion into V_2O_5 thin films: optical, structural and absorption properties. *Surf Interface Anal* 50: 52–58.
174. Julien C, Ivanov I, Gorenstein A (1995) Vibrational modifications on lithium intercalation in V_2O_5 films. *Mater Sci Eng B-Adv* 33: 168–172.
175. Jung H, Gerasopoulos K, Talin AA, et al. (2017) A platform for in situ Raman and stress characterizations of V_2O_5 cathode using MEMS device. *Electrochim Acta* 242: 227–239.
176. Surca A, Orel B (1999) IR spectroscopy of crystalline V_2O_5 films in different stages of lithiation. *Electrochim Acta* 44: 3051–3057.

177. Meulenkam EA, van Klinken W, Schlatmann AR (1999) In-situ x-ray diffraction of Li intercalation in sol-gel V_2O_5 films. *Solid State Ionics* 126: 235–244.
178. Cazzanelli E, Mariotto, Passerini S, et al. (1994) Spectroscopic investigations of Li-intercalated V_2O_5 polycrystalline films. *Solid State Ionics* 70–71: 412–416.
179. Baddour-Hadjean R, Golabkan V, Pereira-Ramos JP, et al. (2002) A Raman study of the lithium insertion process in vanadium pentoxide thin films deposited by atomic layer deposition. *J Raman Spectrosc* 33: 631–638.
180. Baddour-Hadjean R, Navone C, Pereira-Ramos JP (2009) *In situ* Raman microspectrometry investigation of electrochemical lithium intercalation into sputtered crystalline V_2O_5 thin films. *Electrochim Acta* 54: 6674–6679.
181. Levi MD, Lu Z, Aurbach D (2001) Li-insertion into thin monolithic V_2O_5 films electrodes characterized by a variety of electroanalytical techniques. *J Power Sources* 97–98: 482–485.
182. Li YM, Hibino M, Tanaka Y, et al. (2001) Evaluation of Mo-doped amorphous V_2O_5 films as a positive electrode for lithium batteries. *Solid State Ionics* 143: 67–72.
183. Navone C, Baddour-Hadjean R, Pereira-Ramos JP, et al. (2005) High-performance oriented V_2O_5 thin films prepared by DC sputtering for rechargeable lithium microbatteries. *J Electrochem Soc* 152: A1790–A1796.
184. Navone C, Pereira-Ramos JP, Baddour-Hadjean R, et al. (2006) High-capacity crystalline V_2O_5 thick films prepared by RF sputtering as positive electrodes for rechargeable lithium microbatteries. *J Electrochem Soc* 153: A2287–A2293.
185. Donsanti F, Kostourou K, Decker F, et al. (2006) Alkali ion intercalation in V_2O_5: preparation and laboratory characterization of thin films produced by ADL. *Surf Interface Anal* 38: 815–818.
186. Decker F, Donsanti F, Salvi AM, et al. (2008) Li^+ distribution into V_2O_5 films resulting from electrochemical intercalation reactions. *J Brazil Chem Soc* 19: 667–671.
187. Park YJ, Ryu KS, Kim KM, et al. (2002) Electrochemical properties of vanadium oxide thin films deposited by rf sputtering. *Solid State Ionics* 154: 229–235.
188. Liu Y, Li J, Zhang Q, et al. (2011) Porous nanostructured V_2O_5 film electrode with excellent Li-ion intercalation properties. *Electrochem Commun* 13: 1276–1279.
189. Sahana MB, Sudakar C, Thapa C, et al. (2007) Electrochemical properties of V_2O_5 thin films deposited by spin coating. *Mater Sci Eng B-Adv* 143: 42–50.
190. Yu D, Qiao Y, Zhou X, et al. (2014) Mica-like vanadium pentoxide-nanostructured thin film as high-performance cathode for lithium-ion batteries. *J Power Sources* 266: 1–6.
191. Pomerantseva E, Gerasopoulos K, Chen X, et al. (2012) Electrochemical performance of the nanostructured biotemplated V_2O_5 cathode for lithium-ion batteries. *J Power Sources* 206: 282–287.
192. Swiatowska-Mrowiecka J, Maurice V, Zanna S, et al. (2007) Ageing of V_2O_5 thin films induced by Li intercalation multi-cycling. *J Power Sources* 170: 160–172.
193. Pyun SI, Bae JS (1997) Electrochemical lithium intercalation into vanadium pentoxide xerogel film electrode. *J Power Sources* 68: 669–673.
194. Navone C, Baddour-Hadjean R, Pereira-Ramos JP, et al. (2008) A kinetic study of electrochemical lithium insertion into oriented V_2O_5 thin films prepared by rf sputtering. *Electrochim Acta* 53: 3329–3336.

195. Vivier V, Farcy J, Pereira-Ramos JP (1998) Electrochemical lithium insertion in sol-gel crystalline vanadium pentoxide thin films. *Electrochim Acta* 44: 831–839.
196. Miyazaki H, Sakamura H, Kamei M, et al. (1999) Electrochemical evaluation of oriented vanadium oxide films deposited by reactive rf magnetron sputtering. *Solid State Ionics* 122: 223–229.
197. McGraw JM, Bahn CS, Parilla PA, et al. (1999) Li ion diffusion measurements in V_2O_5 and $Li(Co_{1-x}Al_x)O_2$ thin-film battery cathodes. *Electrochim Acta* 45: 187–196.
198. Lu Z, Levi MD, Salitra G, et al. (2000) Basic electroanalytical characterization of lithium insertion into thin, well-crystallized V_2O_5 films. *J Electroanal Chem* 491: 211–221.
199. Li Y, Kunitake T, Aoki Y (2007) Synthesis and Li^+ intercalation/extraction in ultrathin V_2O_5 layer and freestanding V_2O_5/Pt/PVA multilayer films. *Chem Mater* 19: 575–580.
200. Jung KN, Pyun SI (2006) Effect of pore structure on anomalous behavior of the lithium intercalation into porous V_2O_5 film electrode using fractal geometry concept. *Electrochim Acta* 51: 2646–2655.
201. Wang S, Li S, Sun Y, et al. (2011) Three-dimensional porous V_2O_5 cathode with ultra-high rate capability. *Energ Environ Sci* 4: 2854–2857.
202. Li SR, Ge SY, Qiao Y, et al. (2012) Three-dimensional porous $Fe_{0.1}V_2O_{5.15}$ thin film as a cathode material for lithium ion batteries. *Electrochim Acta* 64: 81–86.
203. Mui SC, Jasinski J, Leppert VJ, et al. (2006) Microstructure effects on the electrochemical kinetics of vanadium pentoxide thin-film cathodes. *J Electrochem Soc* 153: A1372–A1377.
204. Navone C, Pereira-Ramos JP, Baddour-Hadjean R, et al. (2005) Electrochemical and structural properties of V_2O_5 thin films prepared by DC sputtering. *J Power Sources* 146: 327–330.
205. Wei Y, Ryu CW, Kim KB (2008) Cu-doped V_2O_5 as a high-energy density cathode material for rechargeable lithium batteries. *J Alloy Compd* 459: L13–L17.
206. Park HK (2005) Manganese vanadium oxides as cathodes for lithium batteries. *Solid State Ionics* 176: 307–312.
207. Grégoire G, Baffier N, Kahn-Harari A, et al. (1998) X-Ray powder diffraction study of a new vanadium oxide $Cr_{0.11}V_2O_{5.16}$ synthesized by a sol-gel process. *J Mater Chem* 8: 2103–2108.
208. Giorgetti M, Berrettoni M, Smyrl WH (2007) Doped V_2O_5-based cathode materials: where does the doping metal go? An X-ray absorption spectroscopy study. *Chem Mater* 19: 5991–6000.
209. Wei Y, Zhou J, Zheng J, et al. (2015) Improved stability of electrochromic devices using Ti-doped V_2O_5 film. *Electrochim Acta* 166: 277–284.
210. Gies A, Pecquenard B, Benayad A, et al. (2008) Effect of silver co-sputtering on V_2O_5 thin films for lithium microbatteries. *Thin Solid Films* 516: 7271–7281.
211. Avellaneda CO, Bulhoes LOS (2006) Optical and electrochemical properties of V_2O_5:Ta sol-gel thin films. *Sol Energ Mat Sol C* 90: 444–451.
212. Panagopoulou M, Vernardou D, Koudouma E, et al. (2017) Tunable properties of Mg-doped V_2O_5 thin films for energy applications: Li-ion batteries and electrochromics. *J Phys Chem C* 121: 70–79.
213. Yu DM, Zhang ST, Liu DW, et al. (2010) Effect of manganese doping on Li-ion intercalation properties of V_2O_5 films. *J Mater Chem* 20: 10841–10846.
214. Ozer N, Sabuncu S, Cronin J (1999) Electrochromic properties of sol-gel deposited Ti-doped vanadium oxide film. *Thin Solid Films* 338: 201–206.

215. Coustier F, Passerini S, Smyrl WH (1997) Dip-coated silver-doped V_2O_5 xerogels as host materials for lithium intercalation. *Solid State Ionics* 100: 247–258.
216. Nam SC, Lim YC, Park HY, et al. (2001) The effects of Cu-doping in V_2O_5 thin film cathode for microbattery. *Korean J Chem Eng* 18: 673–678.
217. Yong W, Zhang HL, Cao HT, et al. (2016) Effect of post-annealing on structural and electrochromic properties of Mo-doped V_2O_5 thin films. *J Sol-Gel Sci Techn* 77: 604–609.
218. Guan S, Wei Y, Zhou J, et al. (2016) A method for preparing manganese-doped V_2O_5 films with enhanced cycling stability. *J Electrochem Soc* 163: H541–H545.
219. Gouda GM, Nagendra CL (2013) Preparation and characterization of thin film thermistors of metal oxides of manganese and vanadium (Mn–V–O). *Sensor Actuat A-Phys* 190: 181–190.
220. Li Y, Yao J, Uchaker E, et al. (2013) Sn-doped V_2O_5 film with enhanced lithium-ion storage performance. *J Phys Chem C* 117: 23507–23514.
221. Etemadi B, Mazloom J, Ghodsi FE (2017) Phase transition and surface morphology effects on optical, electrical and lithiation/delithiation behavior of nanostructured Ce-doped V_2O_5 thin films. *Mat Sci Semicon Proc* 61: 99–106.
222. Sahana MB, Sudakar C, Thapa C, et al. (2009) The effect of titanium on the lithium intercalation capacity of V_2O_5 thin films. *Thin Solid Films* 517: 6642–6651.
223. Lee K, Cao GZ (2005) Enhancement of intercalation properties of V_2O_5 film by TiO_2 addition. *J Phys Chem B* 109: 11880–11885.
224. Kim S, Taya M, Xu C (2009) Contrast, switching speed, and durability of V_2O_5–TiO_2 film-based electrochromic windows. *J Electrochem Soc* 156: E40–E45.
225. Kim S, Taya M (2012) Electrochromic windows based on V_2O_5–TiO_2 and poly(3,3-dimethyl-3,4-dihydro-2H-thieno[3,4-b][1,4]dioxepine) coatings. *Sol Energ Mat Sol C* 107: 225–229.
226. Zhang YF, Hsu CY, Hu CC (2017) Deposition of tungsten-doped V_2O_5 thin films on non-alkali glass substrate by RF magnetron sputtering for thermal insulation. *Key Eng Mater* 732: 16–23.
227. Patil CE, Tarwal NL, Jadhav PR, et al. (2014) Electrochromic performance of the mixed V_2O_5–WO_3 thin films synthesized by pulsed spray pyrolysis technique. *Curr Appl Phys* 14: 389–395.
228. Acharya BS, Nayak BB (2008) Microstructural studies of nanocrystalline thin films of V_2O_5–MoO_3 using X-ray diffraction, optical absorption and laser micro Raman spectroscopy. *Indian J Pure Appl Phys* 46: 866–875.
229. Kim YS, Ahn HJ, Shim HS, et al. (2006) Electrochemical and structural properties of MoO_3–V_2O_5 nanocomposite thin film electrodes for lithium rechargeable batteries. *Solid State Ionics* 177: 1323–1326.
230. Ozer N, Lampert CM (1999) Electrochromic performance of sol-gel deposited WO_3–V_2O_5 films. *Thin Solid Films* 349: 205–211.
231. Madhuri KV, Naidu BS, Hussain OM (2002) Optical absorption studies on $(V_2O_5)_{1-x}$–$(MoO_3)_x$ thin films. *Mater Chem Phys* 77: 22–26.
232. Demets GJF, Anaissi FJ, Toma HE (2000) Electrochemical properties of assembled polypyrrole: V_2O_5 xerogel films. *Electrochim Acta* 46: 547–554.
233. Zhang X, Sun H, Li Z, et al. (2013) Synthesis and electrochromic characterization of vanadium pentoxide/graphene nanocomposite films. *J Electrochem Soc* 160: H587–H590.
234. Wu J, Gao X, Yu H, et al. (2016) A scalable free-standing V_2O_5/CNT film electrode for supercapacitors with a wide operation voltage (1.6 V) in an aqueous electrolyte. *Adv Funct Mater* 26: 6114–6120.

235. Chen W, Mai L, Xu Q, et al. (2003) Synthesis and Li-insertion properties of poly(ethylene-oxide)/V_2O_5 nanocomposite films. *Solid State Phenom* 90–91: 19–24.
236. Murphy DW, Christian PA, DiSalvo FJ, et al. (1979) Lithium incorporation by vanadium pentoxide. *Inorg Chem* 18: 2800–2803.
237. Cocciantelli JM, Ménétrier M, Delmas C, et al. (1995) On the δ → γ irreversible transformation in Li//V_2O_5 secondary batteries. *Solid State Ionics* 78: 143–150.
238. Zhang L, Song J, Dong Q, et al. (2009) Application of V_2O_5 in thin film microbatteries prepared by rf magnetron sputtering. *Adv Mater Res* 79–82: 931–934.
239. Gu G, Schmid M, Chiu PW, et al. (1998) V_2O_5 nanofibre sheet actuators. *Nat Mater* 2: 316–319.
240. Ponzi M, Duschatzky C, Carrascull A, et al. (1998) Obtaining benzaldehyde via promoted V_2O_5 catalysts. *Appl Catal A-Gen* 169: 373–379.
241. Livage J (1991) Vanadium pentoxide gels. *Chem Mater* 3: 578–593.
242. Granqvist CG (2002) *Handbook of inorganic electrochromic materials*, Amsterdam: Elsevier, 295–337.
243. Hirashima H, Ide M, Yoshida T (1986) Memory switching of V_2O_5-TeO_2 glasses. *J Non-Cryst Solids* 86: 327–335.
244. Julien C (1994) Thin film technology and microbatteries, In: Pistoia G, *Lithium Batteries-New Materials-Development and Perspectives*, Amsterdam: Elsevier, 167–237.
245. Bates JB, Dudney NJ, Gruzalski GR, et al. (1993) Fabrication and characterization of amorphous lithium electrolyte thin films and rechargeable thin-film batteries. *J Power Sources* 43–44: 103–110.
246. Nakazawa H, Sano K, Baba M (2005) Fabrication by using a sputtering method and charge–discharge properties of large-sized and thin-film lithium ion rechargeable batteries. *J Power Sources* 146: 758–761.
247. Lee SH, Liu P, Tracy CE, et al. (1999) All-solid-state rocking chair lithium battery on a flexible Al substrate. *Electrochem Solid St* 2: 425–427.
248. Dudney NJ, Neudecker BJ (1999) Soli state thin-film lithium battery systems. *Curr Opin Solid State Mater Sci* 4: 479–482.
249. Oukassi S, Salot R, Pereira-Ramos JP (2009) Elaboration and characterization of crystalline rf deposited V_2O_5 positive electrode for thin film battery. *Appl Surf Sci* 256: 149–155.
250. Navone C, Tintignac S, Pereira-Ramos JP, et al. (2011) Electrochemical behaviour of sputtered c-V_2O_5 and $LiCoO_2$ thin films for solid state lithium microbatteries. *Solid State Ionics* 192: 343–346.
251. Liu P, Zhang JG, Turner JA, et al. (1998) Fabrication of LiV_2O_5 thin-film electrodes for rechargeable lithium batteries. *Solid State Ionics* 111: 145–151.
252. Kim YT, Gopukumar S, Kim KB, et al. (2003) Performance of electrostatic spray-deposited vanadium pentoxide in lithium secondary cells. *J Power Sources* 117: 110–117.
253. Navone C, Baddour-Hadjean R, Pereira-Ramos JP, et al. (2009) Sputtered crystalline V_2O_5 thin films for all-solid-state lithium microbatteries. *J Electrochem Soc* 156: A763–A767.
254. Lee SH, Liu P, Tracy CE (2003) Lithium thin-film battery with a reversed structural configuration SS/Li/Lipon/Li/Cu. *Electrochem Solid St* 6: A275–A277.
255. Navone C, Pereira-Ramos JP, Baddour-Hadjean R, et al. (2010) Lithiated c-V_2O_5 thin-film as positive electrode for rocking-chair solid-state lithium microbattery. *Ionics* 16: 577–580.

256. Gerbaldi C, Destro M, Nair JR, et al. (2013) High-rate V_2O_5-based Li-ion thin film polymer cell with outstanding long-term cyclability. *Nano Energy* 2: 1279–1286.
257. Zeng Y, Gao G, Wu G, et al. (2015) Nanosheet-structured vanadium pentoxide thin film as a carbon- and binder-free cathode for lithium-ion battery applications. *J Solid State Electr* 19: 3319–3328.
258. Mattelaer F, Kobe G, Rampelberg G, et al. (2016) Atomic layer deposition of vanadium oxides for thin-film lithium-ion battery applications. *RSC Adv* 6: 114658–114665.
259. Mattelaer F, Geryl K, Rampelberg G, et al. (2017) Amorphous and crystalline vanadium oxides as high-energy and high-power cathodes for three-dimensional thin-film lithium ion batteries. *ACS Appl Mater Inter* 9: 13121–13131.
260. Chae OB, Kim J, Park I, et al. (2014) Reversible lithium storage at highly populated vacant sites in an amorphous vanadium pentoxide electrode. *Chem Mater* 26: 5874–5881.
261. Ku JH, Ryu JH, Kim SH, et al. (2012) Reversible lithium storage with high mobility at structural defects in amorphous molybdenum dioxide electrode. *Adv Funct Mater* 22: 3658–3664.
262. Sutar MA, Pawar MS, Rendale MK, et al. (2015) Enhancing electrochemical performance of V_2O_5 thin film by using ultrasonic weltering. *IORS J Appl Phys* 7: 41–45.
263. Sandhya GL, Dhananjaya M, Prakash NG, et al. (2017) Structural and supercapacitive performance of V_2O_5 thin films prepared by dc magnetron sputtering. *IOSR J Appl Chem* 10: 64–69.
264. Wruck D, Ramamurthi S, Rubin M (1989) Sputtered electrochromic V_2O_5 films. *Thin Solid Films* 182: 79–85.
265. Talledo A, Andersson AM, Granqvist CG (1990) Electrochemically lithiated V_2O_5 films: An optically passive ion storage for transparent electrochromic devices. *J Mater Res* 5: 1253–1256.
266. Guan ZS, Yao JN, Yang YA, et al. (1998) Electrochromism of annealed vacuum-evaporated V_2O_5 films. *J Electroanal Chem* 443: 175–179.
267. Kaid MA (2006) Characterization of electrochromic vanadium pentoxide thin films prepared by spray pyrolysis. *Egypt J Solids* 29: 273–291.
268. Benmoussa M, Outzourhit A, Bennouna A, et al. (2008) Li^+ ions diffusion into sol-gel V_2O_5 thin films: electrochromic properties. *Eur Phys J Appl Phys* 48: 10502.
269. Rosaiah P, Hussain OM (2013) Electron beam evaporated nano-crystalline V_2O_5 thin films for electrochromic and electrochemical applications, In: Giri P, Goswami D, Perumal A, *Advanced Nanomaterials and Nanotechnology. Springer Proceedings in Physics*, Berlin, Heidelberg: Springer, 143: 485–496.
270. Chen LC, Ho KC (2001) Design equations for complementary electrochromic devices: application to the tungsten oxide–Prussian blue system. *Electrochim Acta* 46: 2151–2158.
271. Sarminio J, Talledd A, Andersson AA, et al. (1993) Stress and electrochromism induced by Li insertion in crystalline and amorphous V_2O_5 thin film electrodes. *Electrochim Acta* 12: 1637–1642.
272. Yoshino T, Baba N, Kouda Y (1987) Electrochromic properties of V_2O_5 thin films colloid-chemically deposited onto ITO glasses. *Jpn J Appl Phys* 26: 782–783.
273. Shimizu Y, Nagase K, Miura N, et al. (1990) New preparation process of V_2O_5 thin film based on spin-coating from organic vanadium solution. *Jpn J Appl Phys* 29: L1708–L1711.

274. Cremonesi A, Bersani D, Lottici PP, et al. (2006) Synthesis and structural characterization of mesoporous V_2O_5 thin films for electrochromic applications. *Thin Solid Films* 515: 1500–1505.
275. Liberatore M, Decker F, Vuk AS, et al. (2006) Effect of the organic–inorganic template ICS-PPG on sol-gel deposited V_2O_5 electrochromic thin film. *Sol Energ Mat Sol C* 90: 434–443.
276. Lin YS, Tsai CW, Chen PW (2008) Electrochromic properties of V_2O_{5-z} thin films sputtered onto flexible PET/ITO substrates. *Solid State Ionics* 179: 290–297.
277. Lu Y, Liu L, Mandler D, et al. (2013) High switching speed and coloration efficiency of titanium-doped vanadium oxide thin film electrochromic devices. *J Mater Chem C* 1: 7380–7386.
278. Kovendhan M, Joseph DP, Manimuthu P, et al. (2015) Prototype electrochromic device and dye sensitized solar cell using spray deposited undoped and 'Li' doped V_2O_5 thin film electrodes. *Curr Appl Phys* 215: 622–631.
279. Rizzo G, Arena A, Bonavita A, et al. (2010) Gasochromic response of nanocrystalline vanadium pentoxide films deposited from ethanol dispersions. *Thin Solid Films* 518: 7124–7127.
280. Abbasi M, Rozati SM, Irani R, et al. (2015) Synthesis and gas sensing behavior of nanostructured V_2O_5 thin films prepared by spray pyrolysis. *Mat Sci Semicon Proc* 29: 132–138.
281. Manno D, Serra A, Giulio MD, et al. (1997) Structural and electrical properties of sputtered vanadium oxide thin films for applications as gas sensing material. *J Appl Phys* 81: 2709–2714.
282. Micocci G, Serra A, Tepore A, et al. (1997) Properties of vanadium oxide thin films for ethanol sensor. *J Vac Sci Technol A* 15: 34–38.
283. Zhuiykov S, Wlodarski W, Li Y (2001) Nanocrystalline V_2O_5-TiO_2 thin-films for oxygen sensing prepared by sol-gel process. *Sensor Actuat B-Chem* 77: 484–490.
284. Raj AD, Mangalaraj D, Ponpandian N, et al. (2010) Gas sensing properties of chemically synthesized V_2O_5 thin films. *Adv Mater Res* 123–125: 683–686.
285. Huotari J, Lappalainen J, Puustinen J, et al. (2013) Gas sensing properties of pulsed laser deposited vanadium oxide thin films with various crystal structures. *Sensor Actuat B-Chem* 187: 386–394.
286. Karthikeyan PS, Dhivya P, Raj PD, et al. (2016) V_2O_5 thin films for 2-propanol vapor sensing. *Mater Today Proc* 3: 1510–1516.
287. Toxicological review of vanadium pentoxide (V_2O_5), 2011. Available from: https://ofmpub.epa.gov/eims/eimscomm.getfile?p_download_id=504127.
288. U.S. National Libray of Medecine, 2005. Available from: https://pubchem.ncbi.nlm.nih.gov/compound/ vanadium_pentoxide#section=GHS-Classification.
289. Eranna G, Joshi BC, Runthala DP, et al. (2010) Oxide materials for development of integrated gas sensors—A comprehensive review. *Crit Rev Solid State* 29: 111–188.
290. Kumar S, Qadir A, Maury F, et al. (2017) Visible thermochromism in vanadium pentaoxide coatings. *ACS Appl Mater Inter* 9: 21447–21456.